SAND2023-03932T

SHOCK RESPONSE SPECTRA OF SHOCK LOADED HEMISPHERE AND PLATE GEOMETRIES

by

James M. Reeves

Submitted in Partial Fulfillment
of the Requirements for the Degree of
Master of Science in Mechanical Engineering
with specialization in Explosives Engineering

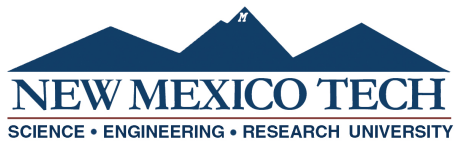

New Mexico Institute of Mining and Technology
Socorro, New Mexico
May, 2023

Sandia National Laboratories
U.S. DEPARTMENT OF ENERGY NNSA

This article has been authored by an employee of National Technology & Engineering Solutions of Sandia, LLC under Contract No. DE-NA0003525 with the U.S. Department of Energy (DOE). The employee owns all right, title and interest in and to the article and is solely responsible for its contents. The United States Government retains and the publisher, by accepting the article for publication, acknowledges that the United States Government retains a non-exclusive, paid-up, irrevocable, world-wide license to publish or reproduce the published form of this article or allow others to do so, for United States Government purposes. The DOE will provide public access to these results of federally sponsored research in accordance with the DOE Public Access Plan https://www.energy.gov/downloads/doe-public-access-plan.

I would like to dedicate this to my parents and family, who always believed the best in everyone and taught me to do the same. I would like the say my thanks to Dr. Hargather for his dedication, support and encouragement of myself and all of us in the Shock and Gas Dynamics Lab. I would like to say thank you to all my friends in the Shock and Gas Dynamics Lab.

James M. Reeves
New Mexico Institute of Mining and Technology
May, 2023

ACKNOWLEDGMENTS

A portion of this work was supported by NNSA/DOE Minority Serving Institution Partnership Program (MSIPP) grant DE-NA0003988. A portion of this work was supported by Sandia National Laboratories. Sandia National Laboratories is a multimission laboratory managed and operated by National Technology and Engineering Solutions of Sandia, LLC., a wholly owned subsidiary of Honeywell International, Inc., for the U.S. Department of Energy's National Nuclear Security Administration under contract DE-NA-0003525.

This dissertation was typeset with LaTeX[1] by the author.

[1]The LaTeX document preparation system was developed by Leslie Lamport as a special version of Donald Knuth's TeX program for computer typesetting. TeX is a trademark of the American Mathematical Society. The LaTeX macro package for the New Mexico Institute of Mining and Technology dissertation format was written by John W. Shipman.

ABSTRACT

The modal response of a system is an important aspect when analyzing transient vibration and shock-loading conditions. This research utilizes the shock response spectrum (SRS) to examine the acceleration response of a steel plate and a steel plate with a hollow hemisphere cap to explosive loading. The 15-cm-diameter hemisphere and 14.2-cm-diameter plate test articles were subjected to explosive loading by 1-gram pentaerythritol tetranitrate (PETN) charges at varying stand-off distances to produce varied shock and impulse loading. Acceleration data were collected using accelerometers at the center line and 4.37 cm off the center line on the circular plate. High-speed schlieren and shadowgraph techniques were utilized to image the shock loading. Calculation of the SRS from the acceleration histories identified a series of frequency peaks which were then compared to modal frequencies determined using finite element analysis (FEA) of the test geometries. SRS of the plate during PETN tests calculated peaks at 2435 and 9742 Hz. Modal analysis of the plate indicates modal frequencies of 1101, 1426, 2411, and 9950 Hz with significant deformation at the center accelerometer location. Frequency analysis on digital image correlation (DIC) data of the plate and response to a calibrated impact hammer indicated a distinct frequency response at 2440 Hz corresponding with the frequencies identified in shock loading SRS and FEA computations. Modal responses of individual components of a multi-component system are found to be present in the modal analysis of the assembled system which indicates the potential to construct a system SRS from individual component SRS profiles.

Keywords: schlieren imaging, shock response spectrum, digital image correlation, finite element analysis, modal analysis

CONTENTS

LIST OF TABLES

LIST OF FIGURES

Figure **Page**

LIST OF NOMENCLATURE

Abbreviations

PETN	Pentaerythritol Tetranitrate
SDOF	Single Degree of Freedom
DIC	Digital Image Correlation
FEA	Finite Element Analysis
SRS	Shock Response Spectrum
ROI	Region of interest
FOV	Field of view
DOF	Depth of field
FFT	Fast Fourier transform
DFT	Discrete Fourier transform
PE	Piezoelectric
PR	Piezoresistive
RSM	Response spectrum method

Terminology

RP-3	Exploding-bridgewire Detonator
Stereo angle	The angle between the optical axes in a stereo DIC setup

Symbols

ζ	Critical damping ratio
Q	Damping coefficient
ω_n	Oscillator natural frequency
Δt	Data sampling time step
ε_x	Refractive angle in x direction
m	Mass of oscillator for spring mass oscillator system
M	Base mass of SDOF oscillator system
e	Mathematical constant, Euler's number
a_1	First order denominator coefficients
a_2	Second order denominator coefficients
b_1	First order numerator coefficients
b_2	Second order numerator coefficients
b_3	Third order numerator coefficients
H	Rational transfer function

c	Damping coefficient of SDOF oscillator
k_n	Spring constant of SDOF oscillator
$\ddot{x}_n$	Acceleration of SDOF oscillator
$\ddot{X}$	Input acceleration of SDOF oscillator system
ω	Rotational velocity
a	Linear acceleration measured in radial direction
r	Distance from center of the accelerometer to center point of rotation
u	Displacement in x direction
v	Displacement in y direction
w	Displacement in z direction
γ	Shear strain
σ	Stress tensor
τ	Shear stress
ϵ	Normal strain
E	Young's modulus
ν	Poisson's ratio

This dissertation is accepted on behalf of the faculty of the Institute by the following committee:

Michael Hargather

Academic and Research Advisor

Jamie Kimberley

Peter Yeh

I release this document to the New Mexico Institute of Mining and Technology.

James M. Reeves May, 2023

CHAPTER 1

INTRODUCTION

1.1 Motivation

Traditional shock and vibration testing is performed to understand a structure's response to transient loading events such as earthquakes, ballistic impacts, and pyrotechnic shock events. A structure's acceleration, velocity, or displacement response to the transient event is typically measured and then analyzed to evaluate the shock and vibration response of the structure. A frequent goal of these tests is to reduce or eliminate unwanted vibrations in the structure [13].

Traditional methods for measuring a structure's response to shock loading in the laboratory commonly utilize mechanical impact testing, pyrotechnic shock, ballistic impacts, and shaker tables to provide transient shock inputs to structures[16, 2]. Analysis of the structure's responses to transient events is typically done by processing the structure's acceleration, velocity, or displacement, which are recorded with instrumentation techniques including accelerometers, photon Doppler velocimetry, or digital image correlation [13]. Recommended data analysis of methods of acceleration histories include calculating the shock response spectrum (SRS), performing a discrete Fourier transform (DFT) or fast Fourier transform (FFT), and integration of acceleration history [13, 2, 16, 14].

The key difference between FFT and SRS outputs is the interpretation of their amplitudes. SRS analysis provides amplitudes representing a physical system's response to an input acceleration [16]. Fourier transforms include the amplitudes of complex components of a data set and require additional processing to calculate a power spectrum [5] to estimate the power distribution of a signal.

One area that has had limited research is the measurement of structural frequency response to explosively-driven shock wave loading. Objects that are subjected to explosively driven shock waves experience a variety of accelerations as a result of the high-frequency shock wave impulse. These accelerations can cause significant frequency response peaks in the object. Explosively driven shock environments present unique challenges when directly measuring a target's response in the laboratory including safety, temporal response, and repeatable loading conditions. Developing an understanding of complex structure frequency responses to varied explosive loading conditions will enable subsequent vibration isolation work. Structures in these environments typically exhibit high accelerations with low velocity changes at high frequencies [2, 13] which requires high

rate and long duration instrumentation measurement approaches.

1.2 Shock Response Spectrum

The shock response spectrum (SRS) was conceptualized by Maurice Biot in 1932 as the response spectrum method (RSM). The RSM was developed for characterizing a building's response to seismic events [4, 29]. Biot's method generalized a multi-leveled building into a vertical system of oscillators with each floor represented by an oscillator of unique resonant frequency with the lowest oscillator experiencing a shear load. Each oscillator then exhibits a unique response to the shear loading based on damping and the resonant frequency of each individual oscillator. The SRS is based on the RSM, but is defined as a maximum response plot for a system of unique resonant frequency single degree-of-freedom (SDOF) oscillators. The SDOF oscillator system experiences a shared transient event and the maximum response of each oscillator is calculated [28, 1, 16]. Response amplitudes in the SRS are commonly expressed in acceleration but can also be expressed in relative velocity or relative displacement [13, 16]. Calculation of the SRS is commonly performed using a modified form of the Smallwood [28] or Kelly-Richman [21] methods.

The application of the SRS is common in assessing a structure's response to pyrotechnic shock events (pyroshock)[1]. Pyroshock events are high amplitude, high frequency, and short duration shock events typical in aerospace vehicles [13]. The use of SRS as a standard method for defining a structural response is codified by the ISO in standard number 18431-4:2007 [17].

1.3 Refractive Imaging

Refractive imaging techniques visualize the variation in the refractive index, n, of a medium. Robert Hooke first described the phenomena of light refraction due to density variations in the atmosphere and liquids, schlieren and shadowgraphy, in the 17th century [27]. August Toepler further developed and popularized these refractive imaging techniques in the 19th century.

Schlieren imaging techniques visualize the gradient of the index of refraction in a medium. A typical schlieren system consists of a point light source located at the focal point of a collimating optic. The parallel light is focused by the second optic back to a point where a knife edge cutoff is placed. A portion of the light is cut off at this point as a result of refractions along the optical path. The light then enters a camera where an image of the light is recorded. The collimating optics are commonly parabolic mirrors or plano-convex lenses.

Figure 1.1 schematically shows a z-type mirror schlieren setup. The curvature of a light ray's path is expressed as:

$$\frac{\partial^2 x}{\partial z^2} = \frac{1}{n}\frac{\partial n}{\partial x} \tag{1.1}$$

The schlieren technique visualizes the first derivative of the refractive index field which can be expressed as the angle ε_x through which the light ray is bent:

$$\varepsilon_x = \frac{1}{n}\int \frac{\partial n}{\partial x}\partial z \tag{1.2}$$

The z-direction is parallel to the collimated light direction, the x-direction is perpendicular to the light ray propagation and ε_x is the refractive angle in the x-direction from the z-axis shown in Figure 1.1. The orientation of the knife edge determines if ε_x or ε_y refractive angle is visualized, as rotating the knife edge to be vertical or horizontal provides this change.

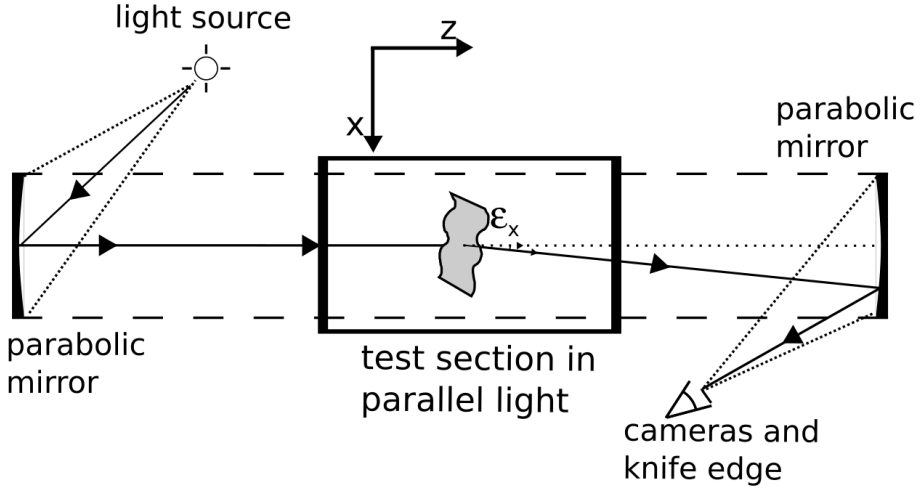

Figure 1.1: Diagram of z-type schlieren setup using parabolic mirrors. A notational light ray is shown propagating through the system and being refracted through an angle ε_x by the gray refractive disturbance.

Schlieren and shadowgraph systems are nearly identical to one another. For shadowgraph imaging, the knife edge is removed from the focal point at the imaging end of the system. Removal of the cutoff allows for visualization of

the second derivative, or Laplacian, of the refractive index field. This technique is useful for imaging sudden changes in the refractive index such as shockwaves or observing the presence of different gas species in the test section. A sample comparison of images using schlieren and shadowgraph imaging techniques can be seen in Figure 1.2. In Figure 1.2, the schlieren image is sensitive to the gradient of the refractive index and is shown as a grayscale effect around the flame. While the shadowgraph displays a distinct boundary layer between the refractive indexes of ambient air and processed air from the candle. The sensitivity of a schlieren system to refractive index gradient makes it the better-suited technique for quantitative measurement of the refractive index in a medium [12].

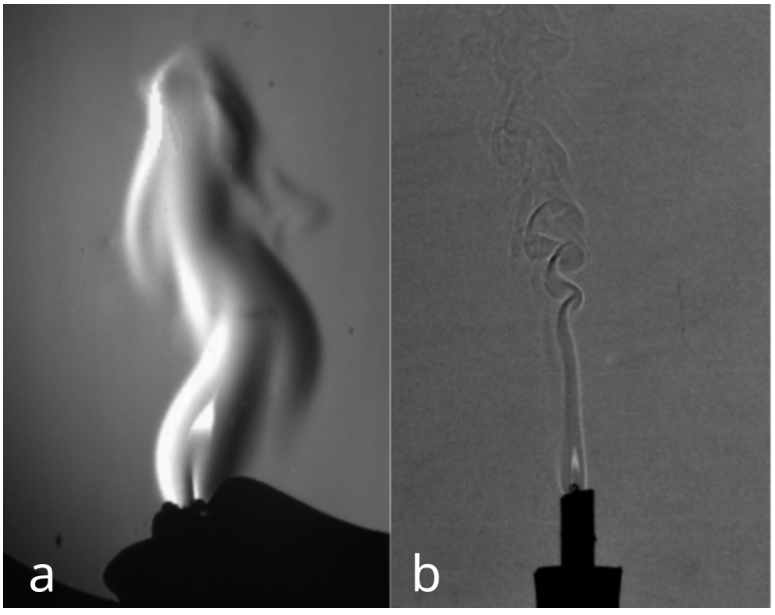

Figure 1.2: Refractive imaging technique examples, (a) schlieren image of a lighter with vertical knife edge and (b) shadowgraph image of a candle

1.4 Finite Element Analysis

Finite element methods (FEM) discretizes a continuous system into a mesh of interconnected elements at nodes. The material properties defined in the model determine how elements in the system deform. The modeled materials are assumed to be isotropic, linear elastic, and exhibit homogeneous behavior. For these models, it is assumed that Poisson's ratio ν, elastic modulus E and shear modulus G are sufficient to describe the material's behavior when a shear, strain, or force is applied. Finite element calculations commonly use three equations based on the theory of elasticity. The three-dimensional equilibrium equation for defining the relationship between internal stress τ_{ij} and external forces b_i is given by:

$$\begin{cases} \frac{\partial \sigma_x}{\partial x} + \frac{\partial \tau_{yx}}{\partial y} + \frac{\partial \tau_{zx}}{\partial z} + b_x = 0 \\ \frac{\partial \tau_{xy}}{\partial x} + \frac{\partial \sigma_y}{\partial y} + \frac{\partial \tau_{zy}}{\partial z} + b_y = 0 \\ \frac{\partial \tau_{xz}}{\partial x} + \frac{\partial \tau_{yz}}{\partial y} + \frac{\partial \sigma_z}{\partial z} + b_z = 0 \\ \tau_{xy} = \tau_{yx}, \tau_{xz} = \tau_{zx}, \tau_{zy} = \tau_{yz} \end{cases} \tag{1.3}$$

The relation between strain and displacement in three dimensions is expressed by:

$$\begin{aligned} u_{xy} &= \frac{\partial v}{\partial x} + \frac{\partial u}{\partial y} \\ u_{yz} &= \frac{\partial w}{\partial y} + \frac{\partial v}{\partial z} \\ u_{zx} &= \frac{\partial u}{\partial z} + \frac{\partial w}{\partial x} \end{aligned} \tag{1.4}$$

With the strain in each direction being: $\varepsilon_x = \frac{\partial u}{\partial x}$, $\varepsilon_y = \frac{\partial v}{\partial y}$, and $\varepsilon_z = \frac{\partial w}{\partial z}$.

The general elasticity matrix D is represented by:

$$D = \begin{bmatrix} \lambda + 2G & \lambda & \lambda & 0 & 0 & 0 \\ \lambda & \lambda + 2G & \lambda & 0 & 0 & 0 \\ \lambda & \lambda & \lambda + 2G & 0 & 0 & 0 \\ 0 & 0 & 0 & G & 0 & 0 \\ 0 & 0 & 0 & 0 & G & 0 \\ 0 & 0 & 0 & 0 & 0 & G \end{bmatrix} \tag{1.5}$$

With $\lambda = \frac{E(1-\mu)}{(1+\mu)(1-2\mu)}$ and $G = \frac{E}{2(1+\mu)}$

These are then used in determining stiffness matrices, nodal displacement, element strain fields, and other system properties. Elements are assigned boundary conditions for calculating responses to external forces, producing a collection of differential equations [20].

For modal analysis using FEA, the system is cyclicly loaded at a specific frequency. Cyclicly loading applies known boundary conditions and the resulting matrices of differential equations can be solved to estimate the response of the system. The FEA package COMSOL, solves large-scale eigenvalue problems based on the ARnoldi PACKage (ARPACK) [6, 19]. The ARPACK is a FORTRAN 77 library developed in 1998 specifically for large-scale eigenvalue problems with the ability to return eigenvalues of real and complex values at a specified maximum and minimum. A secondary eigenvalue solver uses a modified variation of the FEAST algorithm [6, 18]. The FEAST is a residual inverse iterative algorithm able to return specified lowest or largest real and complex eigenvalues [25]. Modal frequency analysis using COMSOL can be performed by specifying a minimum and maximum eigenvalue range. Once the minimum and maximum frequencies are set, an estimated minimum and a maximum number of eigenvalues are set. This method performs a sweeping analysis of modal responses for the mesh system.

1.5 Digital Image Correlation

Digital image correlation (DIC) is a noninvasive measurement method for tracking deformations and displacements of a surface and is commonly used in industry and academia. DIC optically tracks a randomly generated pattern on a surface as deformation and or displacement occurs. The local pattern is identified and matched through the measurement of elements performed by location comparison of sequential in a digital video. By tracking the apparent motion of the pattern, local strain and displacement field are calculated [24, 23]. DIC can be applied as two-dimensional which utilizes a single camera and tracks deformation in a single plane or as three-dimensional which utilizes two cameras in stereo to reconstruct a three-dimensional surface from which three-dimensional deformation can be extracted.

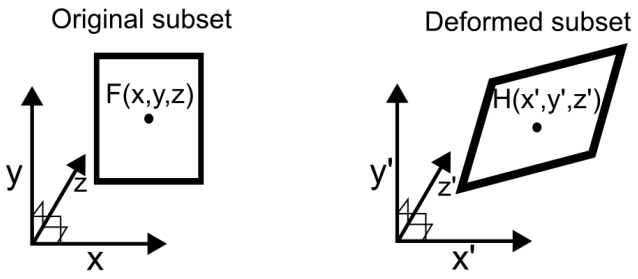

Figure 1.3: Deformation mapping of a subset by DIC. The original image subset (left in coordinate system F) is deformed to the subset shown on the right in coordinate system G

A local region of the pattern being tracked and analyzed is referred to as a subset. The collection of these subsets generates a mapping of the deformed surface. The tracking of elements within a subset is done to determine the deformation mapping of the surface. DIC algorithms allow for both translation and stretching or shear of a subset which enables measurement of muti-directional deformation. An example of deformation mapping in 3D can be seen in Figure 1.3. The relation between the two coordinate systems F and G in deformation mapping can be approximated by Equation 1.6 when deformation is small and aligned with the axis of the camera.

$$x' = x + u + \frac{\partial u}{\partial x}\Delta x + \frac{\partial u}{\partial y}\Delta y + \frac{\partial u}{\partial z}\Delta z \tag{1.6a}$$

$$y' = y + v + \frac{\partial v}{\partial x}\Delta x + \frac{\partial v}{\partial y}\Delta y + \frac{\partial v}{\partial z}\Delta z \tag{1.6b}$$

$$z' = z + w + \frac{\partial w}{\partial x}\Delta x + \frac{\partial w}{\partial y}\Delta y + \frac{\partial w}{\partial z}\Delta z \tag{1.6c}$$

$$\tag{1.6d}$$

Where u, v, and w are translations of the center of the registered element.

Developments in DIC have led to the implementation of multi-camera systems to perform three-dimensional tracking of a surface through similar methods. Three-dimensional (3D) tracking is performed through stereo correlation and stereo triangulation of the pattern elements. The stereo correlation between the two cameras matches the subsets between the paired images recorded from two cameras at the same time. Triangulation builds the full field 3D image by tracking intersecting projection lines between the paired images from the two cameras [30]. An example of this can be seen in Figure 1.4.

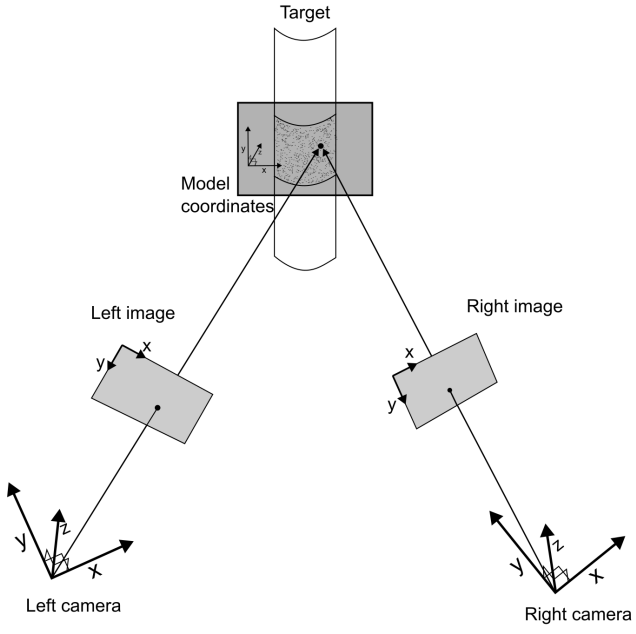

Figure 1.4: Definition of the coordinates and intersecting projection lines used in stereo triangulation on a 3-D surface in DIC.

High-speed imaging paired with DIC allows temporal resolution of deformations and calculation of velocities of deformation and strain rates. This has been shown as a useful method for analyzing dynamic deformation events [11, 26]. The implementation of high-speed cameras and FFT analysis of surface deformation can be performed for high frequencies as the maximum frequency that can be analyzed is dependent on camera frame rate [9, 8].

1.6 Research Objectives

The objective of this thesis is to develop methods for investigating modal responses of a system comprised of simpler geometries and if the constituent mode shapes affect the response of the system. This thesis will explore modal analysis techniques utilizing shock response spectrum (SRS), fast Fourier transform (FFT), finite element analysis (FEA), and digital image correlation (DIC). The goals of this work are to:

- Determine observed frequency peaks in SRS and FFT data from explosive loading tests of hemisphere and plate test articles.
- Exploration of changes in SRS profiles as a function of blast loading conditions by changing the stand off distance of the charge.
- Distinguish the frequency peaks of the assembled hemisphere as modal responses of the individual components.
- Implement DIC as a method of calculating SRS and comparing measured peaks to accelerometer data and modal frequencies in FEA models.

CHAPTER 2

METHODS

2.1 Experimental Setup

Shock loading tests using pentaerythritol tetranitrate (PETN) were performed, with high-speed schlieren and images recorded simultaneously with acceleration histories and pressure data. Test geometries consisted of a flat circular steel plate and the same plate inserted into a hollow steel hemisphere cap. The two geometries had a total of 19 tests at varying standoff distances as listed in Tables 2.2 and 2.1.

The test setup consisted of Z-type mirror schlieren with a gantry system centered in the test section to suspend for the test article and PETN charge as shown in Figure 2.1. The gantry system was constructed from extruded aluminum supports with a base width of 2.4 meters and a max suspension height of 2.6 meters. The wide gantry base provided enough clearance for the handling of charges and all supporting equipment to be outside the view of the imaging system. Construction of the schlieren system used a pair of parabolic mirrors as the light collimation method with a test section spanning between two optical tables. The distance between optical tables provided clearance for the gantry system, handling of PETN safely, and removal of shock wave reflections from ground effects and any surrounding equipment.

Table 2.1: Matrix of PETN shock loading tests for hemisphere geometry

Shot #	Standoff (cm)	PETN mass (g)	% TMD
3	16.4	0.986	94
4	16.7	0.986	94
6	16.4	-	-
7	10.5	-	-
8	10.9	0.971	93
9	-	1.004	96
10	15.5	1.016	97
11	16.2	1.029	98
19	30	1.031	98
20	30	1.042	99

Table 2.2: Matrix of PETN shock loading tests for plate geometry

Shot #	Standoff (cm)	PETN mass (g)	% TMD
1	16.4	0.996	95
2	16.7	0.997	95
12	15	1.011	96
13	15	1.033	98
14	20	1.037	99
15	20	1.025	98
16	14.7	1.043	99
17	15.4	1.040	99
18	20.2	1.041	98

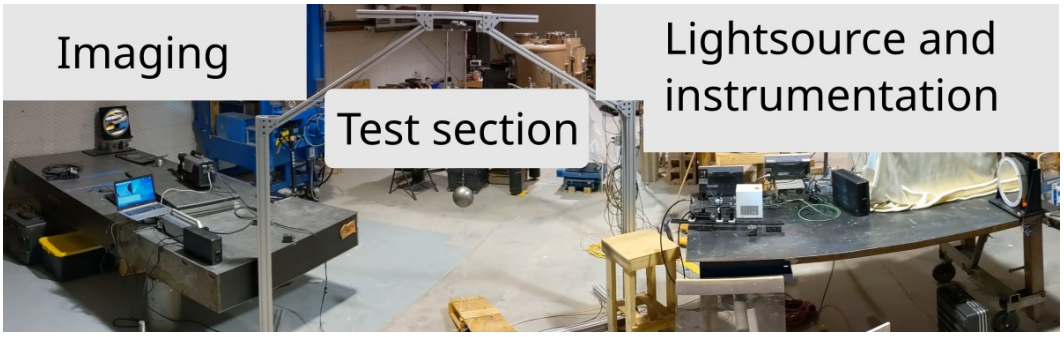

Figure 2.1: Alignment setup for Z-type schlieren

Test articles consisted of a flat circular plate of 14.6 cm diameter and 6 mm thickness made of 1018 mild steel. Tests included a hollow hemispherical cap into which the plate was secured using three eye bolts. The bolts were located along the outer edge of the plate with 120^o separation between each. The hemisphere was made of the same 1018 mild steel as the plate with a diameter of 15.24 cm and a wall thickness of 3 mm. Accelerometers were positioned on the flat plate at the center and 4 cm off the center using mounting blocks. The orientation of accelerometers was normal to the plate surface with measured positive acceleration being measured in the same direction.

2.2 Instrumentation

Data on the shock wave strength was measured using multiple methods: accelerometers, free field pressure gauges, and imaging with shadowgraph and schlieren techniques. The shock wave loading was measured using acceleration histories collected by accelerometers mounted on the opposing side impacted by the shock and later analyzed by SRS methods. Near-and-far field pressure data

was collected by free field pressure gauges oriented to face the charge without being visible in the schlieren system. Imaging of the shock loading event was done by a pair of high-speed cameras, one utilizing shadowgraph and the other schlieren imaging. A trigger line from the FS-17 was used to trigger the Stanford Research Systems delay generator DG535 to send a trigger signal to the cameras, laser, accelerometers, and pressure gauges. The delay generator provided adjustable delays to the cameras to account for shock wave travel time before loading the test article and laser pulse duration time as this varied with frame rate. The instrumentation wiring block diagram is shown in Figure 2.2.

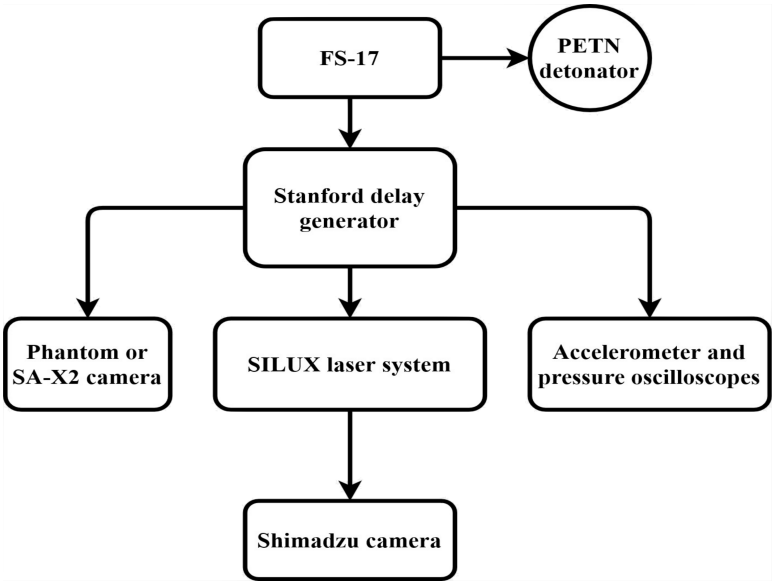

Figure 2.2: System triggering diagram

2.2.1 Accelerometers

Acceleration data was collected using Endevco accelerometers models 7270A-2K, 7270AM7-6K, and 7270A-60K, paired with tri-axial mounting blocks model 7970 as seen in Figure 2.3. Mounting blocks were manufactured out of Titanium alloy with modal frequencies outside the frequency range of interest. Signal conditioning was done using Endevco 4418 battery-powered conditioners. These conditioners also assisted in reducing electrical noise from the FS-17 fireset during the initiation of the detonators. Installation of accelerometers was done using Endevco mounting screws, washers, and a glycerine-based coupling gel. Securing accelerometers to the mounting block required no more than 0.9 Nm torque to avoid an induced DC offset from applying excessive force to the internal piezoresistive circuit. The selection of piezoresistive (PR) accelerometers was for their high case resonant frequencies [31] of 100 kHz and the polarization flipping that occurs in piezoelectric (PE) accelerometers at high accelerations [10].

2.2.2 Pressure gauges

Free field pressure gauges were implemented with standoffs of 56 cm and 38 cm from the explosive charge. These positions were outside of the high-speed camera's field of view. PCB model 137B23B with a rating to 345 kPa was used for far-field pressure measurement. PCB model 137B24B with a rating to 1724 kPa was used for near-field pressure measurement. The choice of pressure gauges was determined using Winter's pressure estimations at these standoff distances from 1-gram PETN charges [33].

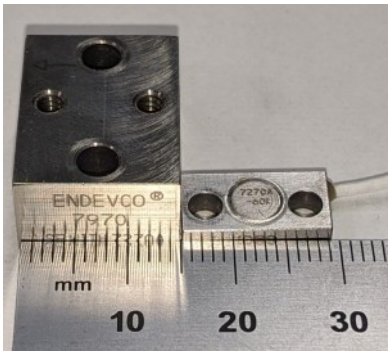

Figure 2.3: Endevco accelerometer and triaxial mounting block

2.2.3 High-speed refractive imaging

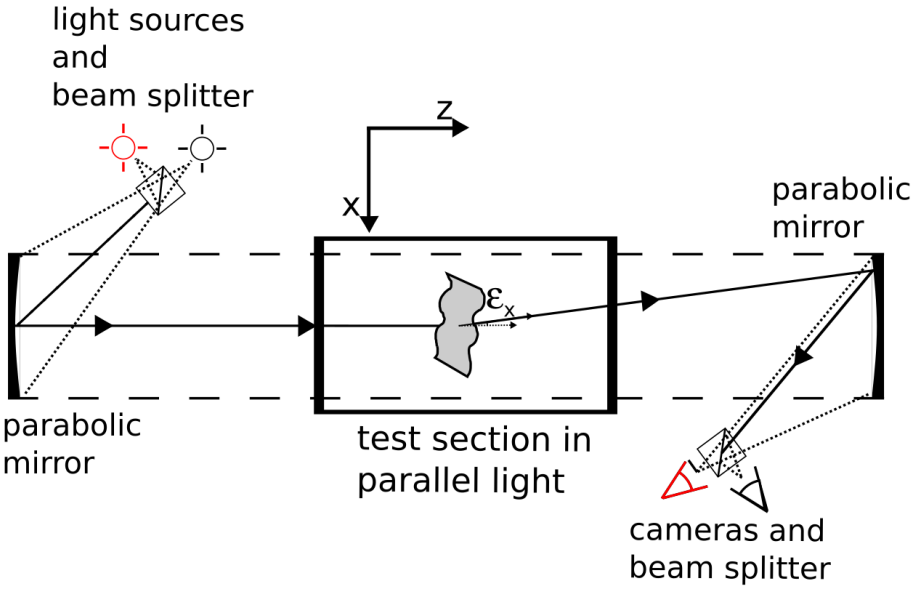

Figure 2.4: Diagram of z-type schlieren and shadowgraph setup using parabolic mirrors for light collimation. Beam splitters at light sources and cameras to combine and split light sources

A schematic of the z-type shadowgraph and schlieren setup is shown in Figure 2.4. This z-type method implements a dual camera system to image the same field of view with schlieren imaging and shadowgraph simultaneously with separate light sources and different frame rates. The setup consisted of paired 31-cm-diameter parabolic mirrors with 1.9-m focal lengths. Beam-splitting cubes were used to combine the light sources into a common optical path through the schlieren system and then separate the light before entering individual cameras.

The optical train begins with the two light sources, a SugarCUBE white LED light and a SILUX coherent spoiled 480 nm laser, both directed towards a beam-splitting cube that aligns the light to a common optical path. The combined light is directed toward a condensing lens with an adjustable iris at the condensing lens's focal point to create a finer-point light source. The iris is located at the first mirror's focal point, creating a folding angle between the iris and the collimated light. The collimated light is directed toward the second mirror, passing through the test section, and is refocused at a second beam splitter with a folding angle equal to the first. The second beam splitter directs the light toward the two cameras. A 480 nm band pass filter is used for the camera designated to use the 480 nm light source. Neutral density filters for both cameras are placed as needed. A

Shimadzu HPV-X2 camera was used with the SILUX laser light source at 1 million fps for early-time imaging of shock impacting the test article surface. This event was approximately 100 - 200 μs in duration which necessitated the high frame rate. The second camera recorded at a slower frame rate for a longer duration. The cameras varied between Phantom v711 and Photron SA-X2 with frame rates of 40,000-50,000 fps and a total imaging duration of 5-6 ms using the white LED SugarCUBE as the light source.

2.3 Explosive Shock Loading

Common shock loading methods include drop impact, attached pyrotechnic shock (pyroshock), impact hammers, or shaker tables [13]. Here explosions in free air are performed at varying stand-off distances from the models as the loading source.

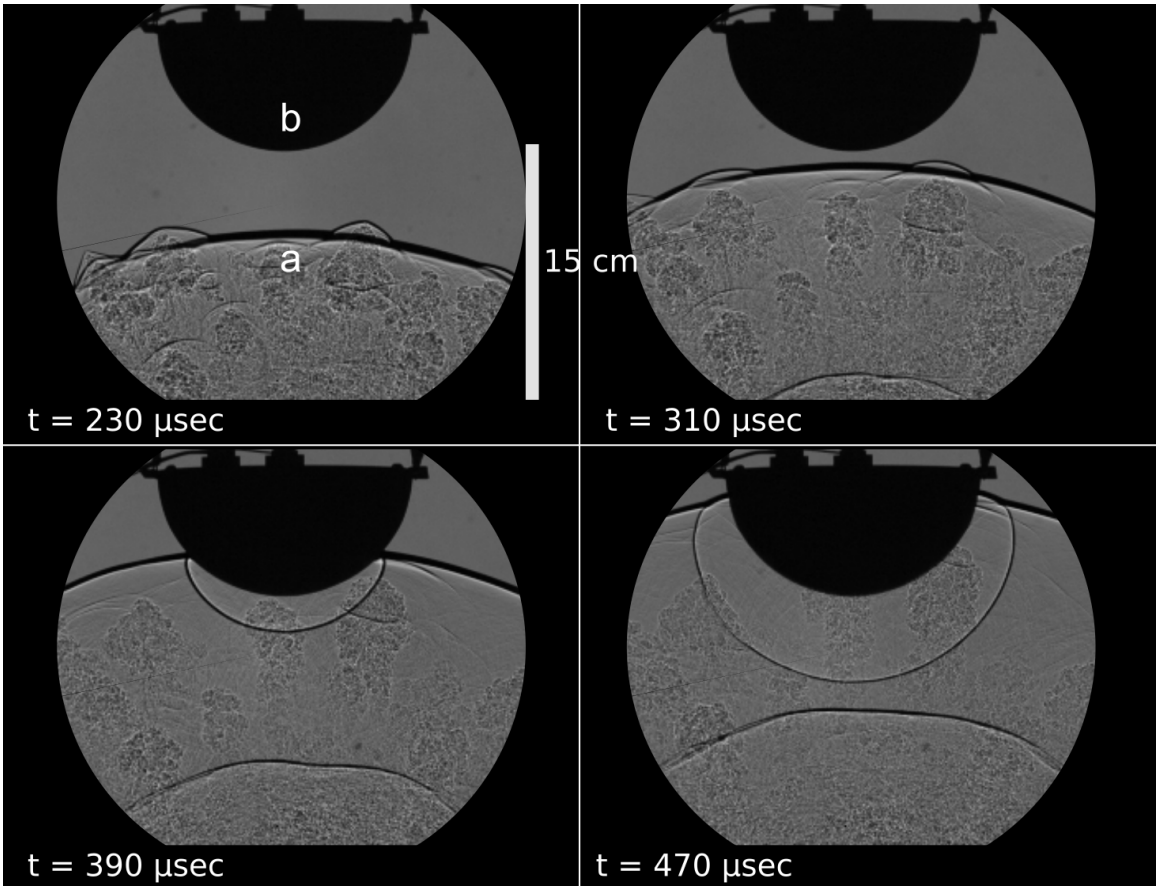

Figure 2.5: Shadowgraph images of hemisphere test article shock loaded by 1-gram PETN shock wave. The (a) explosion is below the field of view and the shock wave is the black arc moving upward toward the (b) hemisphere.

For these tests, shock loading was performed using 1-gram PETN pellets pressed to near theoretical max density (TMD) of 1.77 g/cm^3 [7]. Formation of the PETN charges is done through static uniaxial pressing using preformed dies as shown in Figure 2.6. Procedures for pressing are included in Appendix A. A 15-minute settling period occurred when the desired pressure was reached and maintained for the 15-minute duration. The dies used required a pressing force of 1450 $\pm$25 kg to produce a desired density near 1.7 g/cm^3. PETN charge preparations were done on the day of tests with a center-positioned RP-3 detonator held in place using a thin layer of cyanoacrylate adhesive on the bare face of the RP-3 detonator. A completed assembly of a charge and detonator can be seen in Figure 2.7. RP-3 detonators contain an additional 30 mg of PETN for the explosive train and were considered a negligible amount of additional explosives for these tests. The leads for the RP-3 detonator are rigid enough to support the PETN charge during alignment and testing. The charge is suspended using the gantry system with the spherical surface of the charge facing the test article, this is to ensure as symmetrical of a shock front as possible for the shock load source.

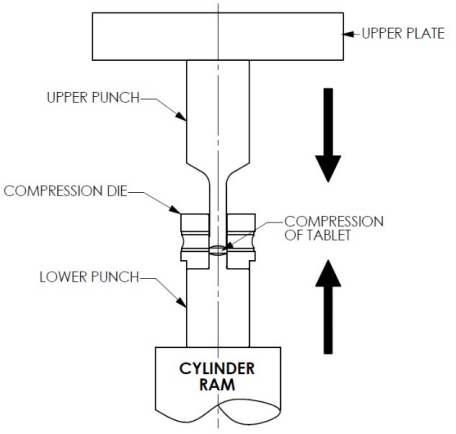

Figure 2.6: Assembled pressing dies manufactured by Natoli

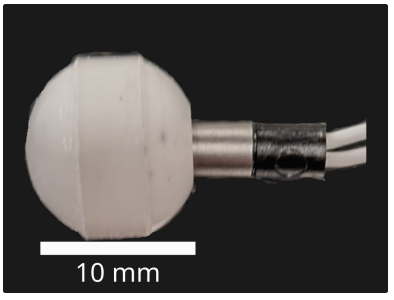

Figure 2.7: 1-gram PETN charge prepared for detonation by RP-3 detonator

2.4 Shock Response Spectrum Calculation

Calculation of shock response spectra in this research was done using the modified method introduced by Smallwood [28]. The basis of the shock response spectrum in Smallwood's calculation can be visualized as a transient event applied to the system of single-degree oscillators of increasing natural frequencies and the corresponding response acceleration history of each oscillator is then calculated. Here the Smallwood method is adopted because it is more suitable for a broader frequency range than the Kelly-Richman method [28, 21].

The method to simulate the response of each oscillator utilizes Equations:

$$Y(z) = \sum_{n=0}^{\infty} y[n] z^{-n} \tag{2.1}$$

$$H(z) = \frac{b_1 + b_2 z^{-1} + b_3 z^{-2}}{1 + a_1 + a_2 z^{-1}} \tag{2.2}$$

$$a_1 = 2e^{-\zeta\omega_n \Delta t} cos(\omega_n \sqrt{1-\zeta^2}) \tag{2.3}$$

$$a_2 = -e^{-2\zeta\omega_n \Delta t} \tag{2.4}$$

$$b_1 = 1 - \frac{e^{-\zeta\omega_n \Delta t} sin(\omega_n \sqrt{1-\zeta^2})}{\omega_n \sqrt{1-\zeta^2}} \tag{2.5}$$

$$b_2 = 2e^{-\zeta\omega_n \Delta t} \left(\frac{sin(\omega_n \sqrt{1-\zeta^2}}{\omega_n \sqrt{1-\zeta^2}} - cos(\omega_n \sqrt{1-\zeta^2}) \right) \tag{2.6}$$

$$b_3 = e^{-2\zeta\omega_n \Delta t} - \frac{e^{-\zeta\omega_n \Delta t} sin(\omega_n \sqrt{1-\zeta^2})}{\omega_n \sqrt{1-\zeta^2}} \tag{2.7}$$

$$X(z) = H(z) Y(z) \tag{2.8}$$

The Smallwoood method processes the acceleration history x as a function of time through the 1-D filter in Equation 2.2. The damping coefficient ζ is standardized to be an undamped system with ζ = 0.05, or the equivalent Q factor of 10 [28, 13]. Where the Q factor is another dimensionless representation of how damped a system is and can be expressed as:

$$Q = \frac{1}{2\zeta} \tag{2.9}$$

The process is performed on each individual potential natural frequency ω_n that is considered. A series of natural frequencies are generated at equidistant frequency points on a logarithmic scale based on the minimum frequency of interest and the maximum frequency feasible based on the input time step Δt. The first natural frequency used here was $\omega_n = 1$Hz. The time step Δt for the acceleration data sampling rate is specified. Each coefficient in Equations 2.3 - 2.7 is then calculated for each natural frequency with ζ remaining a constant. The 1-D filter in Equation 2.2 is then applied to the acceleration time history resulting in the simulated acceleration history H for the oscillator at the given natural frequency. The natural frequency is incremented and the process is repeated to produce the system response at each natural frequency of interest. The resulting acceleration histories of a select number of oscillators can be seen in Figure 2.8 and continuing to simulate the frequencies between the select oscillators produce the completed system response. Once the simulation of the oscillators is completed, the maximum acceleration of each oscillator is extracted and plotted to produce the SRS as shown in Figure 2.9.

The derivation of the coefficients in Equations 2.3 - 2.7 was performed by Irvine [16] and the standardized formulation can be found in ISO 18431-4:2007 [17].

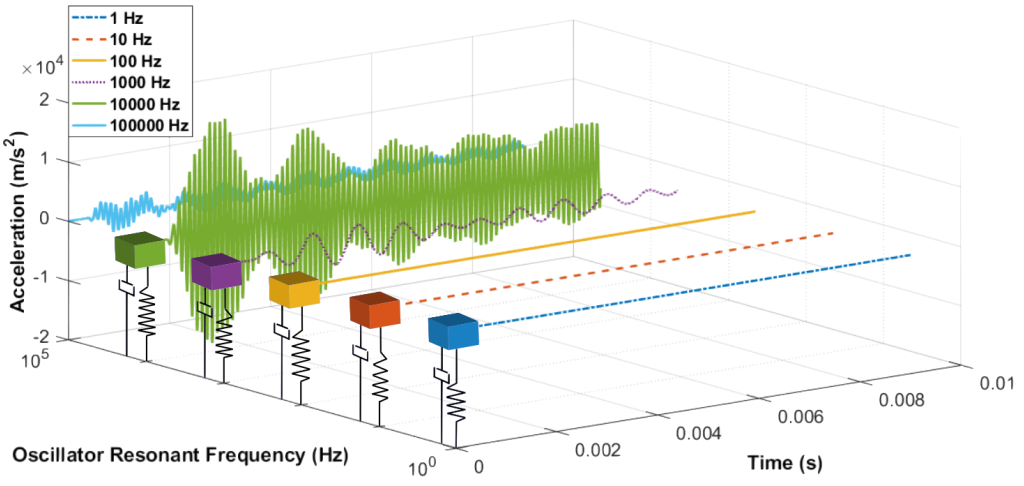

Figure 2.8: Deconstruction of a shock response spectrum displaying response acceleration histories of 6 SDOF oscillators of natural frequencies: 1 Hz, 10 Hz, 100 Hz, 1000 Hz, 10 kHz, and 100 kHz.

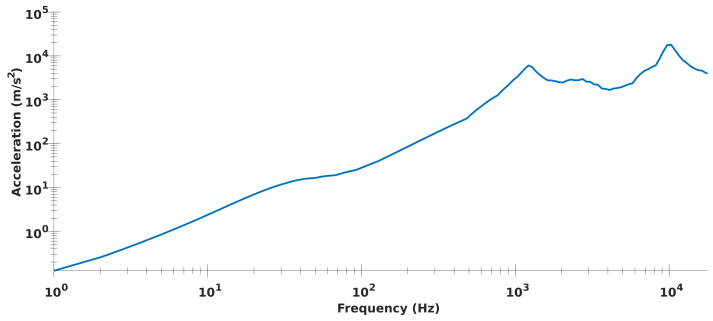

Figure 2.9: The completed SRS from the deconstructed plot displaying 6 SDOF oscillator responses.

2.5 Data Filtering and Processing

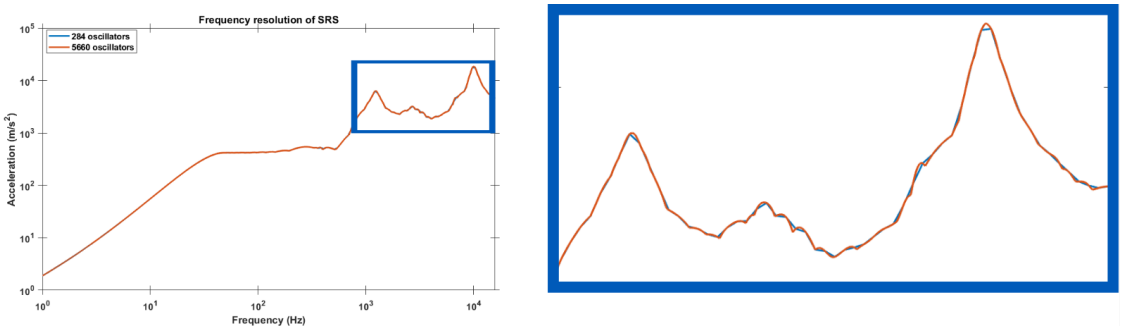

Figure 2.10: SRS results of 284 and 5660 logarithmically spaced natural frequency oscillators calculated from 15 cm standoff assembled hemisphere PETN detonation test.

Calculation of the SRS for the data presented in this research was done using a system of 284 SDOF oscillators of logarithmically increasing resonant frequency. Presented here is the comparison of the SRS of the 284 oscillator system to one estimating the response of a 5660 oscillator system using the same data set from the 15 cm standoff assembled hemisphere test. The comparison between the two systems is shown in Figure 2.10 with the 284 system in blue and 5660 system overlaying in orange. The response of the two systems is comparable in the entire frequency range and provides additional frequency resolution if desired at the cost of computation time with either system appearing to be a viable method.

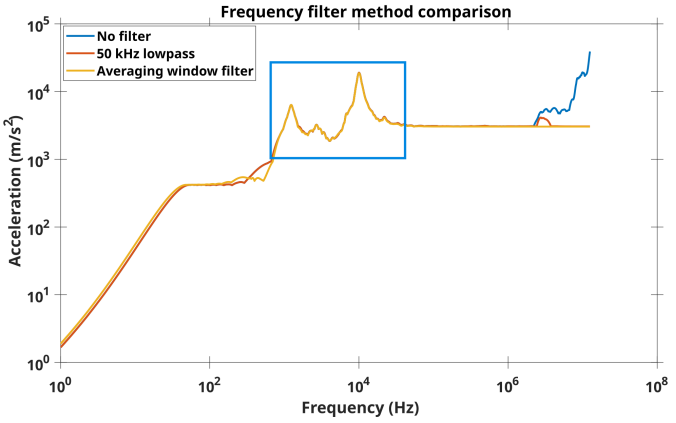

Figure 2.11: SRS results of different filtering methods of acceleration history.

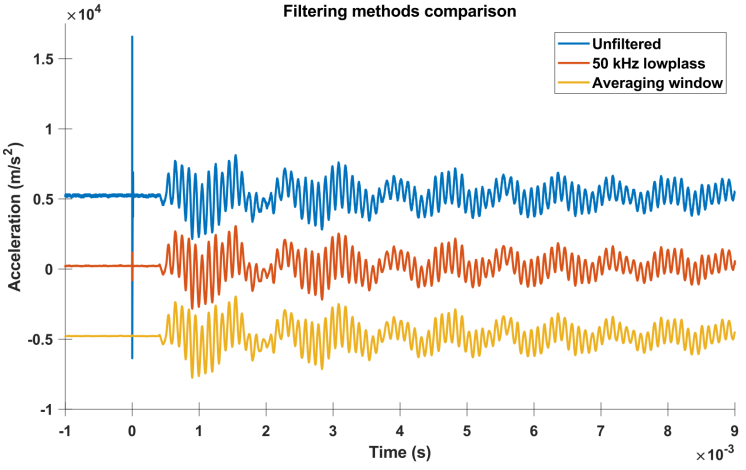

Figure 2.12: Frequency filter comparison between unfiltered data, 50 kHz lowpass, and averaging window

Filtering methods of frequencies introduced by instrumentation for this work are presented in Figure 2.11 and is suggested in literature [15]. Filtering of these artificial peaks consisted of a 50 kHz lowpass filter or an averaging window filter. Both methods did not display any influence on the calculated SRS in the frequency band of interest, 1 Hz - 10 kHz. The introduction of filtering was primarily to determine if variation in instrumentation sampling had an influence on the frequency band of interest. The resulting filtered SRS profiles compared to an unfiltered SRS indicates no concern about whether data was filtered or not. A benefit of filtering acceleration history before processing was the removal of a voltage spike introduced by the FS-17 as the RP-3 was detonated as seen in Figure 2.12

2.6 Baseline Impact Hammer Experiments

Supporting tests were performed on target geometries to measure the SRS response to a clibrated impatct hammer loading. These tests included accelerometer measurements and Digital Image Correlation (DIC) measurements of the circular steel plate surface motion during impact loading by a calibrated impact hammer.

Lab scale DIC tests were done using a pair of Photron Mini UX100 cameras in a stereo setup as seen in Figure 2.13. Once the setup was in place, calibrations were performed using a target of known dimensions with a known dot pattern size in place of the test article and oriented in varying directions and orientations [9]. Once calibrated analysis of the paired images was performed by VIC-3D after indicating regions of interest, size of subset regions and duration of the video to be analyzed.

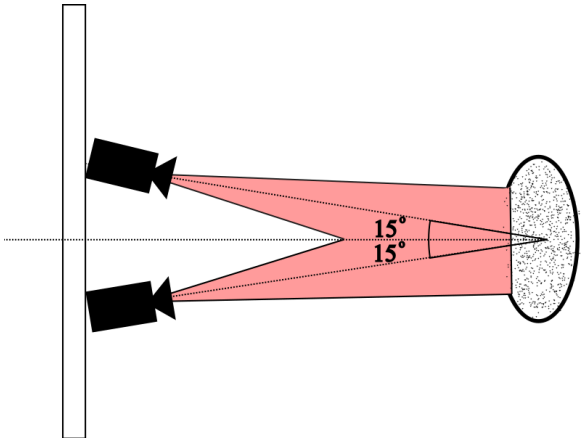

Figure 2.13: A top-down view of a DIC schematic with cameras in the same focal plane highlighted in red and a stereo angle of 15^o.

Following setup procedures outlined in [3], a stereo angle of $15^o \pm 1^o$ off of the center line was used. A top-down schematic of the DIC setup is shown in Figure 2.13. Each camera was paired with a 55mm lens focused at the center point of the suspended steel plate with an applied speckle pattern shown in Figure 2.14. The test article was suspended in the focal plane of the cameras such that the orientation of the steel plate was normal to the cameras and the center of the plate was directed down the center line between both cameras.

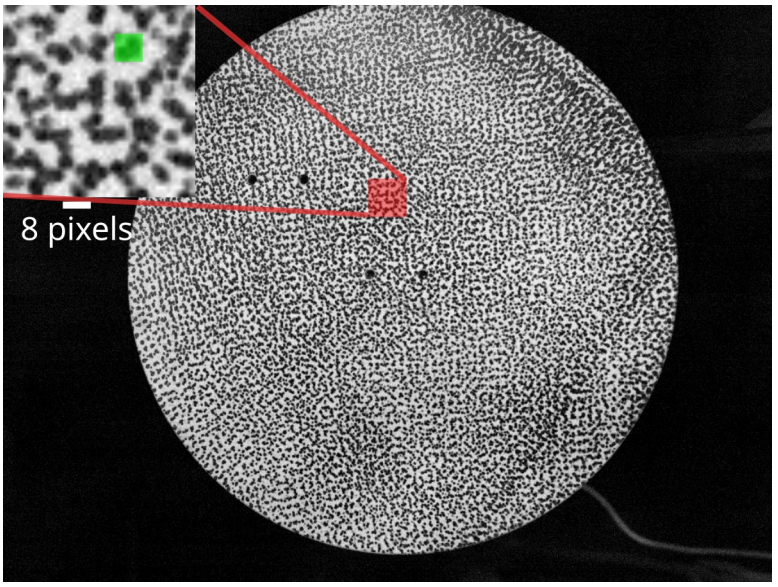

Figure 2.14: Speckle pattern on plate test article with speckle pattern average size of 6 pixels

Cameras were rigidly mounted to a tripod isolated from the optical table and synchronized using VIC Snap recording at 16000 fps. An accelerometer was mounted to the far side of the plate for a direct comparison of accelerometer and DIC data. Frequency analysis of the DIC data was performed to display plate deformation as a function of frequencies. Figure 2.15 is a sample of frequency analysis showing a peak acceleration at the center of the plate for a frequency input of 2440 Hz.

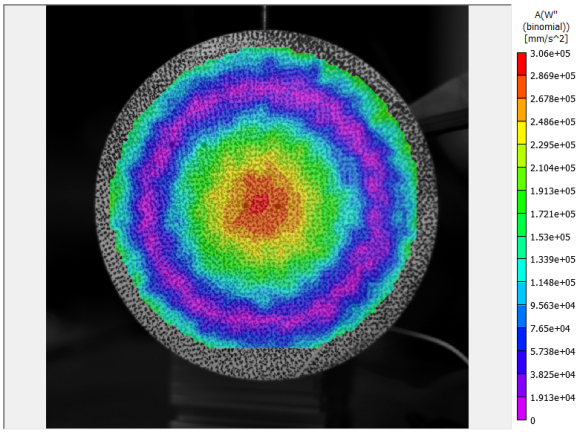

Figure 2.15: DIC analysis of circular plate displaying relative acceleration at 2440 Hz

Stereo system calibration was performed with the provided 7mm calibration target and VIC-Snap calibration package. Collected DIC data was processed us-

ing VIC-3D with a given step size of 9 and a subset size of 18 was used after outlining the area of interest. The area of interest used for the plate was the full plate surface coated in a speckle pattern shown in Figure 2.14The resulting surface shapes were calculated by VIC-3D and further processed using the frequency analysis tool. The center point of the plate was a selected tracking point to extract position and acceleration data from for comparison to the accelerometer on the opposite side.

Loading of the plate was performed using PCB 086C02 impulse force hammer. Impulse force hammers provide a known and repeatable loading of the plate. The impacting tip of the hammer can be interchanged with different materials to provide an adjustable pulse width. These impact tests used the provided steel tip and applied a loading pulse width of 0.3 ms. Impacting occurred at 1 to 2 cm above the center of the plate.

2.7 Finite Element Analysis

Modeling of modal responses of the steel circular plate and steel hemisphere cap was performed using the COMSOL Multiphysics package. The purpose of finite element analysis (FEA) was to model the geometries in order to determine which modal frequencies deformed at locations on circular plates observable by accelerometers. Two FEA models were examined, the first being on the circular plate and accelerometer mounts and the second being the complete assembly with hemisphere cap, circular plate, and accelerometer mounts.

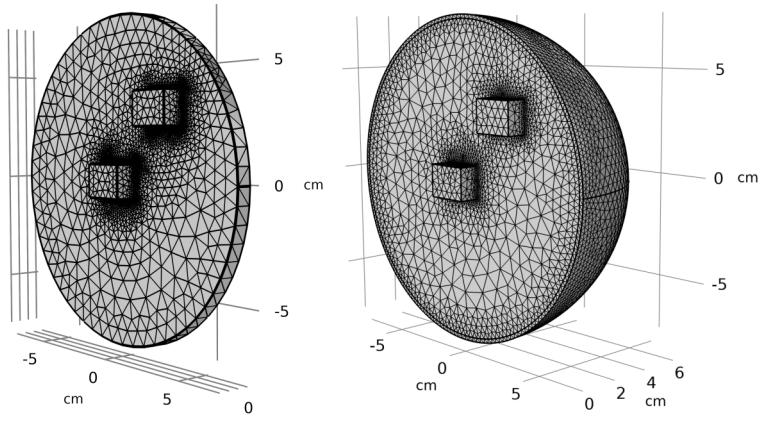

Figure 2.16: COMSOL mesh models of plate (left) and hemisphere (right) test articles. The accelerometers and mounting blocks are the rectangular prism shapes affixed to the plates.

FEA models of a hollow steel hemisphere, flat circular steel plate, and two titanium rectangular blocks were made. Both the hemisphere and steel plate were made of 1018 mild steel with the following dimensions: 15.2 ± 0.1 cm diameter hollow hemisphere, wall thickness 3.1 ± 0.1 mm, mass of 446 ± 0.5g and a circular plate with a diameter of 14.6 ± 0.1cm, thickness of 6.3 ± 0.1mm and mass of 1357 ± 0.5g. Attached to the outer surface of the plate are two titanium 6AI-4V triaxial accelerometer mounting blocks, $15.24mm \times 20.32mm \times 9.15mm$ in dimension, each with a mass of 10.9 ± 0.1g. The accelerometers are excluded from the FEA models because the additional mass was considered negligible in relation to the assembled plate, hemisphere, and mounting blocks. For reference, the completed hemisphere and plate have a mass of 1.803kg, mounting blocks each have a mass of $12.5 \pm 0.1g$ and each accelerometer has a mass of $0.23 \pm 0.01g$, making the mass of each accelerometer is nearly 3.9 orders of magnitude smaller than the mass of the hemisphere and plate assembly. The inclusion of the mounting blocks was done as their mass accounted for $2.8 \pm 0.1\%$ the total mass.

FEA models were generated using a physics-controlled mesh of free tetrahedral shells. The max mesh element size is 0.817 cm and the minimum size of 0.597 cm. Displacement fields were set as quadratic serendipity. Frequency analysis was performed using ARPACK region search method over a series of 10 studies. Each study was performed in 1000 Hz frequency intervals. An external loading of 250 N was applied to the forward face of each geometry. This loading force was determined from near-field pressure data taken by free-field pressure gauges during explosive loading tests.

CHAPTER 3

RESULTS

Acceleration histories of the hemisphere and circular plate test articles were collected and analyzed using SRS methods. Each test article was explosively loaded using PETN charges placed at standoff distances ranging from 10 to 30 cm. Each PETN charge was pressed to near TMD 1.778 g/cm^3 with masses of $1 \pm .04$ grams. The resulting SRS analysis of these accelerations displayed similar frequency peaks between both test articles and some frequency peaks unique to each test article. Further investigation of these peaks was done using FEA and DIC methods to better resolve the observed frequency peaks and possible corresponding modal responses of the geometries. FEA was performed as a sweeping method to estimate modal responses that may be observed at accelerometer locations for a range of frequencies from $1 - 10000$ Hz.

3.1 Gram-scale PETN Detonation Tests

Experiments were performed to load the plate and hemisphere models with varied explosive loading. The explosive loading was changed by varying the standoff distance of the charge to the model. Variation of standoff distances provides a method to vary the shock load amplitude, as the peak overpressure decays with increased standoff distance. The tests performed are summarized in Tables 2.1 and 2.2 for the hemisphere and plate tests respectively. Each test utilized high-speed imaging to visualize the shock impact and the accelerometers to collect the acceleration data which was converted to the SRS. Figure 3.1 an image series from Test 16 listed in Table 2.2 showing the shock impingement and reflection. The accelerometers can be seen on the top side of the plate (away from the blast in the images.

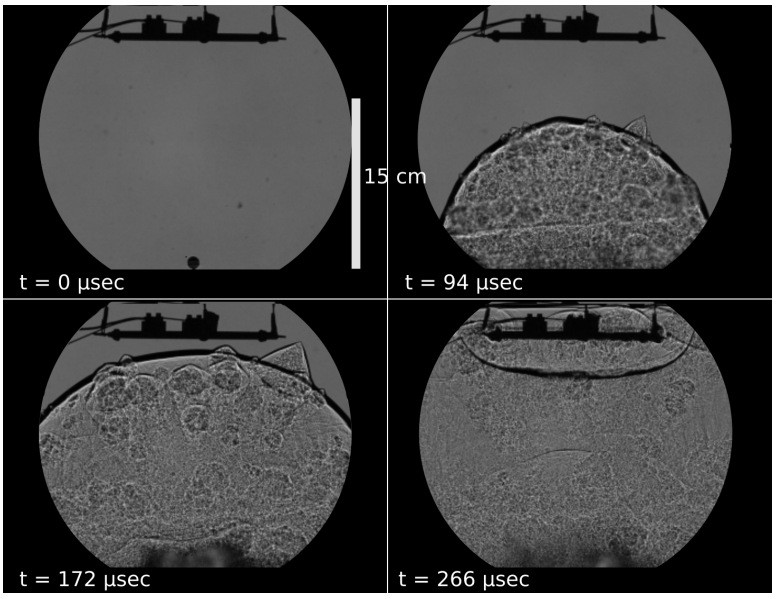

Figure 3.1: Shadowgraph imaging of 14.2 cm diameter steel plate shock-loaded by 1-gram PETN charge

From the impacting shock as seen in Figure 3.1, acceleration histories are collected then analyzed using SRS methods. The acceleration histories are also processed with a FFT analysis to identify frequency response peaks. Notable frequency peaks for each test article configuration are determined by identifying shared peaks of SRS profiles at differing standoff distances and the scaled average of the SRS profiles. Scaling and averaging of SRS plots is done for both test geometries to better distinguish shared frequency peaks, additional averaging of closely grouped standoff tests was also done for examination of lower amplitude peaks. Primary frequency peaks remained grouped within a 10% margin of the peak frequencies determined by the scaled average.

Acceleration responses of the plate test article produced a range of frequency peaks in their corresponding SRS profiles with similar peaks present in the corresponding FFTs. Standoff distances of 14.7, 15, 16.4, 16.6, and 20 cm resulted in similar frequency peaks with variance remaining within 5%. An upper bound of 10 kHz was chosen when considering frequency peaks in SRSs and FFTs to maintain consistency with FEA and remain in a frequency range well outside the influence of internal time step variation of the oscilloscope.

The oscilloscope used for these tests has a maximum step variation of 2 ns across a sample length of 3 ms introducing frequency peaks in frequency ranges 100 kHz-1 MHz. Accelerometers used in these tests have a reported frequency response range of $0 - 100$ kHz with a $\pm 5\%$ confidence. The Nyquist frequency is given as half the sampling rate, 50 kHz. The introduced frequency noise at the 100 kHz-1 MHz range can be ignored as it is well outside the Nyquist frequency and frequency range on interest $1 - 10$ kHz.

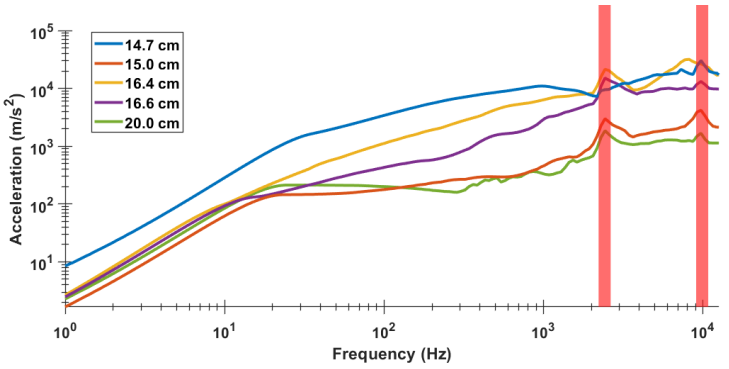

Figure 3.2: SRSs of plate test article at varying standoff distances with primary frequency peaks 2435 Hz and 9743 Hz indicated in red

The collection of response spectra from accelerations at the center point of the plate surface indicates two primary peaks at 2435 Hz and 9742 Hz, shown in Figure 3.2. The FFT of acceleration history from the 15 cm standoff test confirms peaks at 2400 Hz and 9700 Hz in Figure 3.3 and to be within 2% of the SRS values.

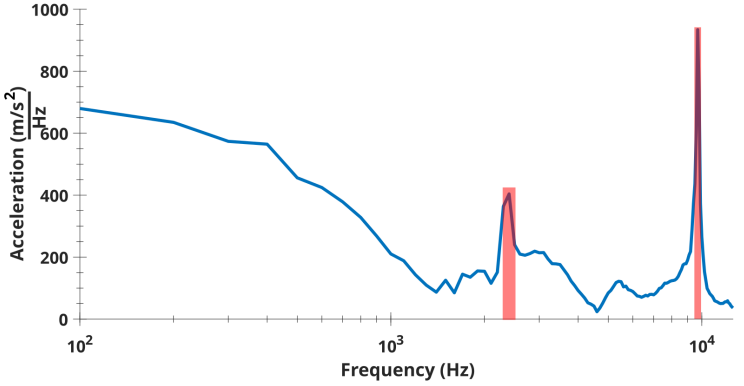

Figure 3.3: FFT of 15 cm plate detonation test acceleration history displaying frequency peaks 2400 Hz and 9700 Hz highlighted in red

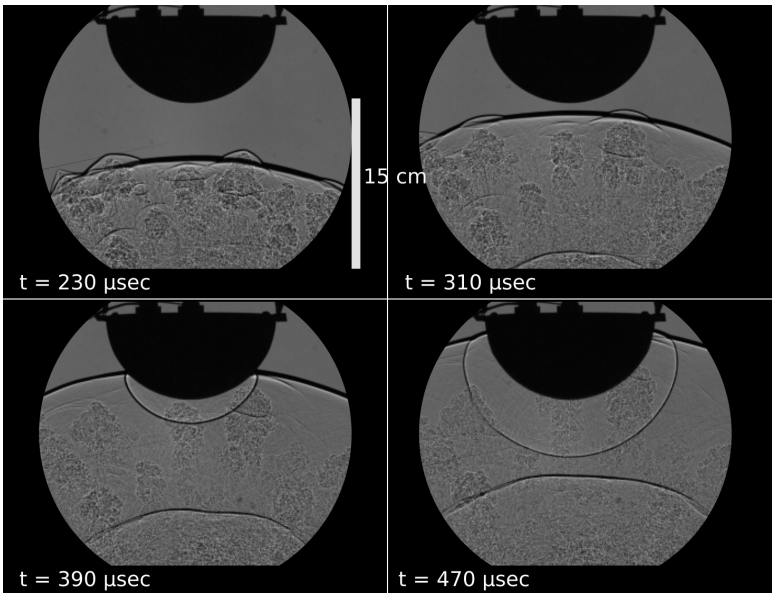

Figure 3.4: Shadowgraph imaging of 15 cm diameter assembled hemisphere test article shock-loaded by 1-gram PETN charge

Similar PETN detonation tests of the assembled hemisphere test article are seen in Figure 3.4. Acceleration histories of the assembled hemisphere were processed in the same manner as the plate test article using SRS and FFT. The hemisphere was positioned at standoff distances of 10.5, 15.5, 16.4, 16.7, and 30 cm as a means to vary the strength of the shock load applied to the test article. These acceleration histories produced the SRS profiles presented in Figure 3.5. A similar trend of shared frequency peaks is present as in the plate test article. The SRS frequency peaks at 9741 Hz and 2733 Hz were present in the assembled hemisphere. The hemisphere model peak at 9741 Hz is in close agreement with the plate model peak at 9742 Hz and the peak at 2733 Hz is more than 10% higher than the plate model peak at 2435 Hz.

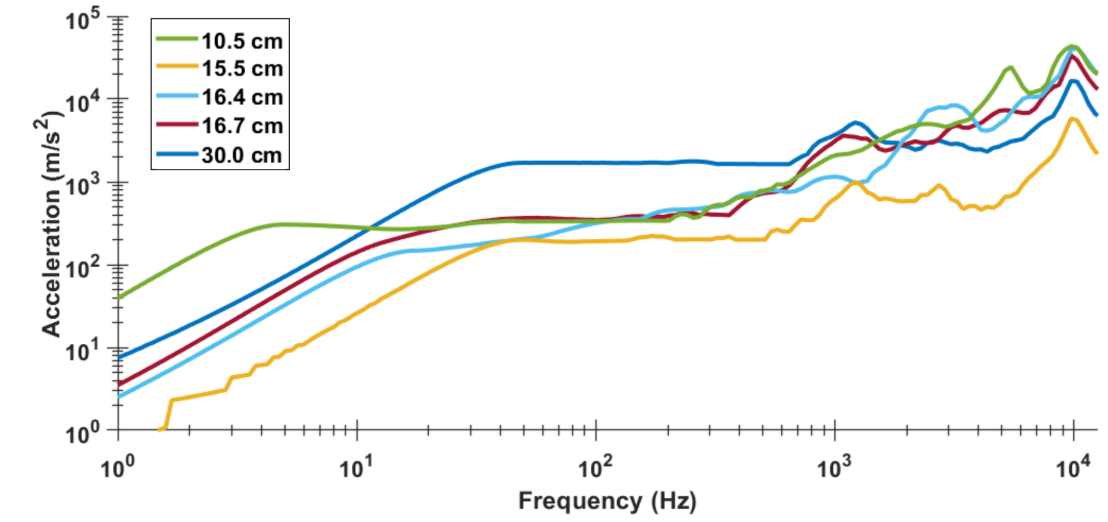

Figure 3.5: Assembled hemisphere test article SRS profiles from standoff distances: 10.5, 15.5, 16.4, 16.7, and 30.0 cm.

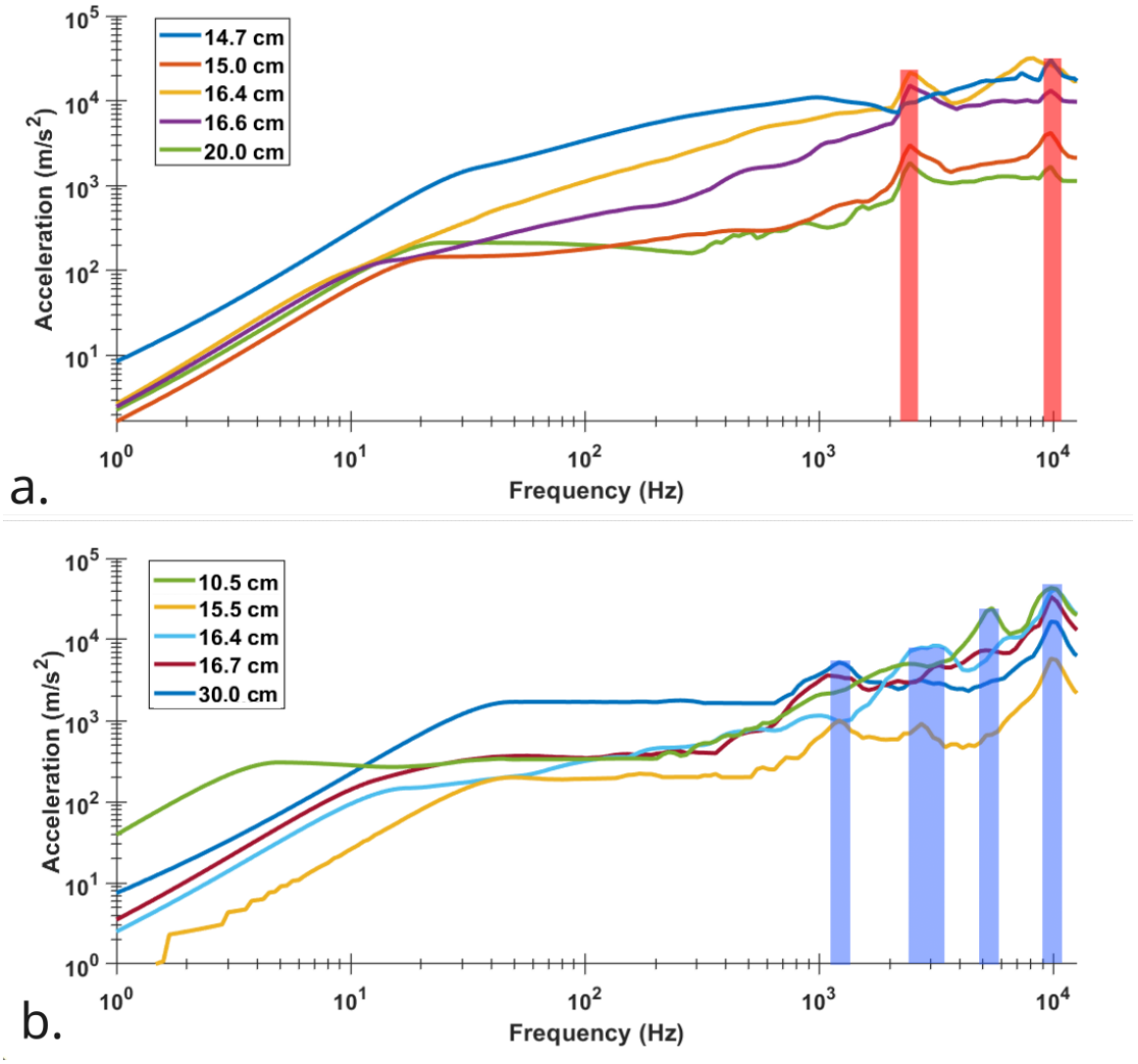

Figure 3.6: Collection of SRS profiles of (a) plate and (b) assembled hemisphere test articles. Plate frequency peaks are indicated in red at 2435 Hz and 9742 Hz. Hemisphere frequency peaks are indicated in blue at 1218 Hz, 2734 Hz to 3251 Hz, 5468 Hz, and 9741 Hz.

The collection of SRS profiles for plate and assembled hemisphere The regions highlighted in red indicate frequency peaks of 2435 Hz and 9742 Hz present in both the assembled hemisphere and plate. Regions highlighted in blue indicate frequency peaks 1218 Hz, 2734 to 3251 Hz, and 5468 Hz present in the assembled hemisphere. This commonality of frequency peaks between the plate and assembled hemisphere along with frequency peaks unique to the assembled hemisphere suggests these frequency peaks are influenced by the individual components of the entire geometry.

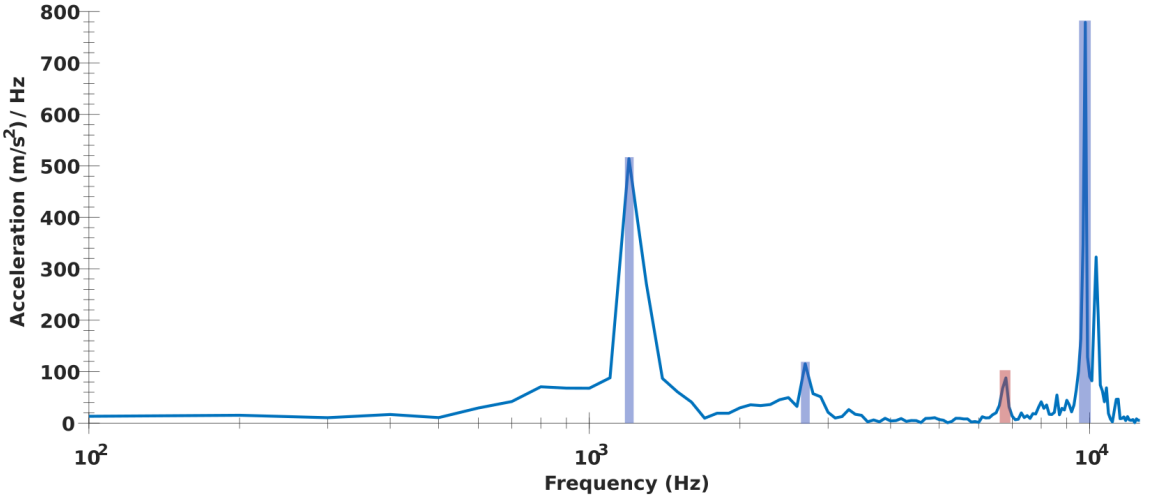

Figure 3.7: The FFT of the assembled hemisphere acceleration history at 30 cm standoff.

The FFT on the assembled hemisphere produces similar frequency peaks as observed in SRS analysis of the assembled hemisphere. Frequency peaks from the FFT of the 30 cm standoff test indicate peaks at 1200, 2700, and 9800 Hz highlighted in blue. These peaks determined through FFT fall within 3% of those determined through the scaled and averaged SRS of the assembled hemisphere. The outlier in FFT analysis is a 6800 Hz peak highlighted in red. This peak is not present in the scaled averaged SRS nor the SRS of the same test data as a prominent peak. It is shown as a minor inflection point on the rising slope up to the 9742 Hz peak. This is likely due to the low amplitude response as observed in the FFT. With the 6800 Hz peak being 20% higher frequency than the predicted peak in the scaled average SRS peak at 5467 Hz, both are considered to be unrelated.

Table 3.1: Frequency peaks collected from SRS analysis of plate and hemisphere geometries in Hz.

Geometry	Peak 1	Peak 2	Peak 3	Peak 4	Peak 5
Plate	2435	9742	-	-	-
Hemisphere	1218	2734	3251	5468	9741

Shock wave pressure data was collected at varying standoff distances to identify various shock parameters. Pressure data was used to determine peak pressure, pulse duration, and impulse at varying standoffs. Calculation of impulse was performed using methods outlined by Winter [33]. A summary of the pressure data collected and the parameters mentioned can be seen in Table 3.2. The peak pressures presented decrease with standoff distance and the duration

of this pressure pulse increases with the standoff distance. The trend of a decaying impulse as standoff distance increases is shown here and presented by Winter [33].

Table 3.2: Pressure data parameters from pressure gauges at varying standoff distances. Parameters from data collected by Winter [33] indicated by (*).

Standoff (cm)	Peak pressure (kPa)	Duration (ms)	Impulse (kPa s)
10.4*	5114	0.08	0.051
14.5*	1901	0.14	0.026
16.4*	945	0.16	0.021
20*	471	0.15	0.017
38	253	0.25	0.006
46	177	0.28	0.005
55	145	0.30	0.004
57	121	0.31	0.004
77	93	0.34	0.003

3.2 Modal Analysis Using FEA

Modal analysis through FEA over the range of 1 Hz to 10 kHz was performed separately for the plate, hemisphere cap, and fully assembled hemisphere model. The determination of appropriate modal frequencies to be presented was dependent on deformation locations. Plate deformation regions of interest focused on the accelerometer mount located at the center of the plate. The hemisphere cap deformation region of interest was the contact surface where the circular plate was inserted into. Assembled hemisphere deformation regions of interest were at the center accelerometer mount location.

Individual FEA on the accelerometer mounting block was performed but no modal response in the frequency band of interest for this research was identified. Both mounting block and accelerometers were calculated to have a minimum resonant frequency above 100 kHz.

A broad sweep of modal responses between 1 Hz to 10 kHz was performed. Modes displaying large deformation at accelerometer locations were selected for comparison to SRS and FFT results from PETN detonation tests. Table 3.3 is the list of presented modal responses for each geometry. A range of modal responses was calculated and the presented modes show large deformation at the center accelerometer location and notable displacement of the accelerometer block itself. Comparing the modal frequencies of the isolated hemisphere and plate, there was minimal overlap in frequencies of interest between the components.

Table 3.3: FEA modal frequencies of individual geometries and assembled test article

	Frequencies (Hz)			
Plate	1101	1426	2411	9950
Hemisphere cap	1328	2749	3133	5409
Assembled hemisphere	1145	2763	5430	9697

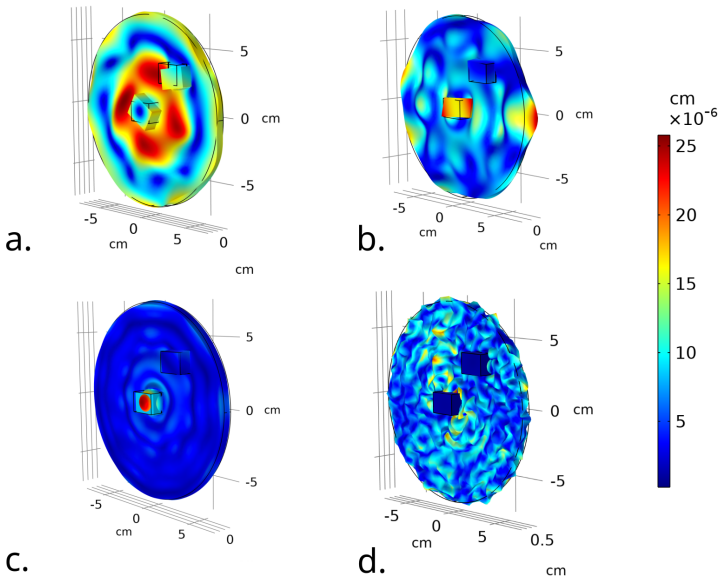

Figure 3.8: Mode shapes displaying out-of-plane displacement at excitation frequencies: (a) 1101 Hz (b) 1426 Hz (c) 2411 Hz (d) 9950 Hz.

The presented mode shapes in Figure 3.8 were selected as they displayed a maximum deformation at the center accelerometer location and at a frequency near those observed in the plate SRS. Mode shapes at 2411 Hz and 9950 Hz fall within 1% and 3% of the scaled average SRS peaks at 2435 Hz and 9743 Hz respectively from Figure 3.6. The two remaining modes, 1101 Hz and 1426 Hz are inferred from weaker trends between the SRS profiles collected. The 20 cm standoff plate test displayed an additional lower frequency peak at 1534 Hz. A gradual rise near 1024 Hz is observed in the 14.7 cm, 15.0 cm, and 16.6 cm standoff tests These peaks are both within 7% and 8% of the modes at 1101 Hz and 1426 Hz respectively.

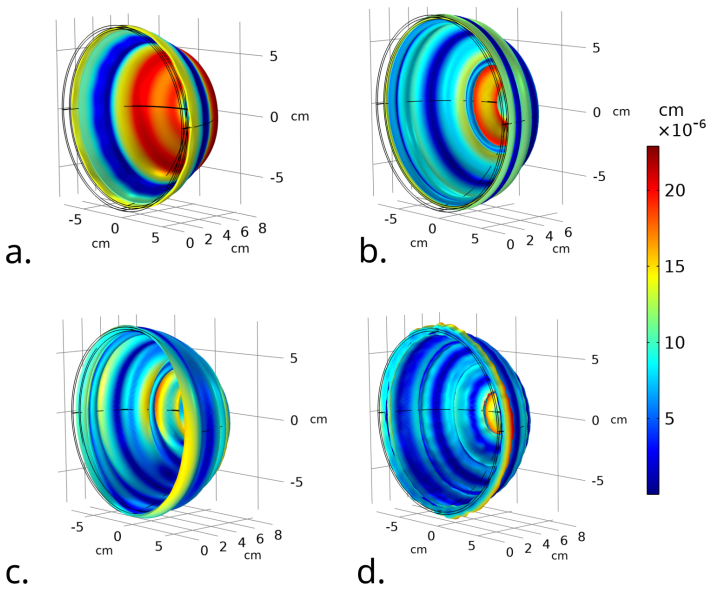

Figure 3.9: Hemisphere cap mode shapes displaying deformation along the contact surface between the plate and the cap at excitation frequencies: (a) 1328 Hz (b) 2749 Hz (c) 3133 Hz (d) 5556 Hz

The hemisphere cap mode shapes in Figure 3.9 were selected for their deformation region being the contact surface with the plate geometry during explosive loading tests. Analysis of the hemisphere cap determined modes of interest being frequencies 1328 Hz, 2749 Hz, 3133 Hz, and, 5556 Hz as shown in Figure 3.9. The close proximity of hemisphere mode 1328 Hz to plate mode 1426 Hz makes these difficult to distinguish in the assembled geometry SRS. Isolated hemisphere modes at 2769 Hz and 3133 Hz with plate mode 2411 Hz are considered as the local plateau in the SRS from 2400 Hz to 3200 Hz for the assembled hemisphere in Figure 3.6.

Table 3.4: Frequencies of interest determined from SRS and FEA for plate, cap, and assembled hemisphere geometries.

	Frequency (Hz)			
Experimental plate	2435	9742	-	-
FEA plate	2411	9950	-	-
Experimental cap	not tested			
FEA cap	1328	2749	3133	5556
Experimental full hemisphere	1218	2734	5468	9742
FEA full hemisphere	1145	2763	5430	9691

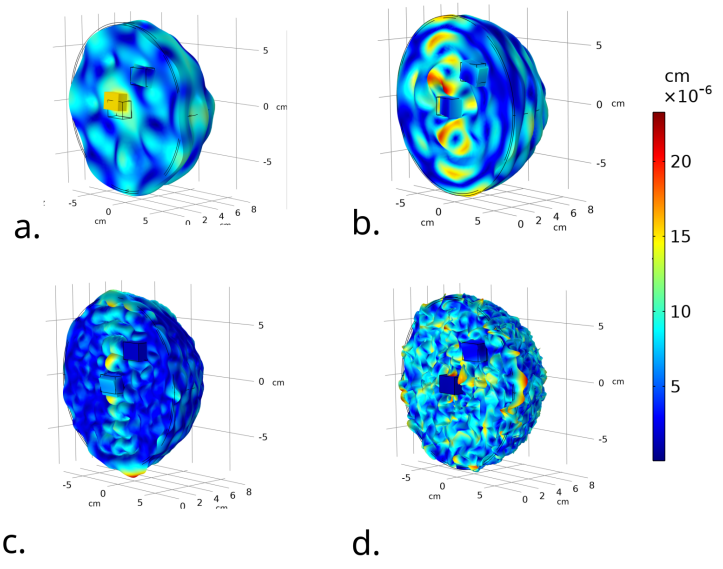

Figure 3.10: Assembled hemisphere modal responses displaying deformations at center accelerometer mount position: (a) 1145 Hz (b) 2763 Hz (c) 5430 Hz (d) 9691 Hz

The FEA of the assembled hemisphere determined modal responses with deformation at the center accelerometer location at 1145 Hz, 2763 Hz, 5430 Hz, and 9691 Hz as shown in Figure 3.10. Comparing FEA mode frequencies to frequency peaks of the scaled average SRS of the hemisphere, all FEA peaks are within 3% of the SRS peaks previously mentioned in Figure 3.6

3.3 Calibrated Hammer Impact

DIC during loading of the test article by calibrated impact hammer provides a method to visually confirm deformation mode shapes non-intrusively. Tracking the center point of the plate allowed for the extraction of the acceleration which is compared to the acceleration history measured on the opposing side by the accelerometer. Mapping of the plate surface allows for the exploration of modal responses which are not directly measurable by accelerometers, as many mode shapes do not deform at the accelerometer location.

Surface deformation tracking using DIC and frequency analysis of extracted acceleration data determined a primary frequency peak at 2440 Hz displaying deformation at an accelerometer location as shown in Figure 3.11. A 3D rendering of the mode shape at 2440 Hz calculated by Vic 3D can be seen in Figure 3.12. This rendering illustrates similar deformations as observed in the plate mode 2411 Hz determined by FEA in Figure 3.8. This frequency response peak is observed in all three methods, SRS, FEA, and DIC.

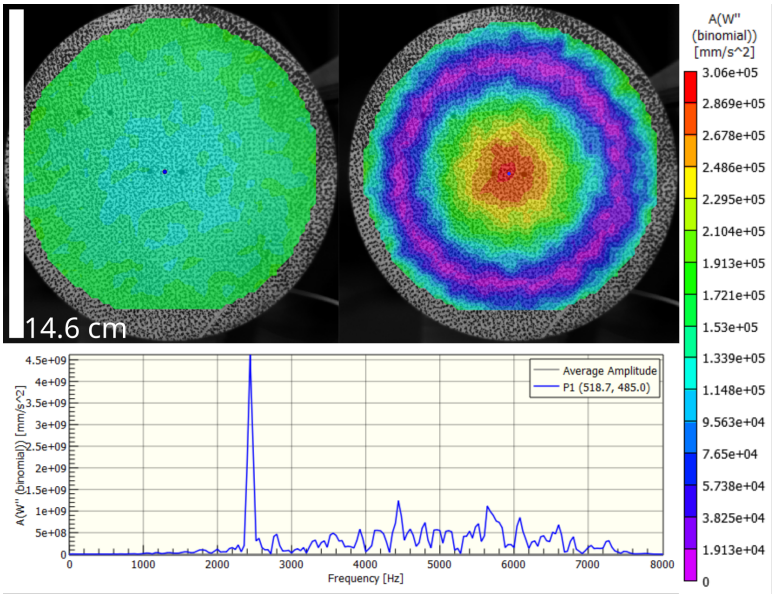

Figure 3.11: Plate overlay intensity plot of FFT analysis on DIC data at 2440 Hz peak

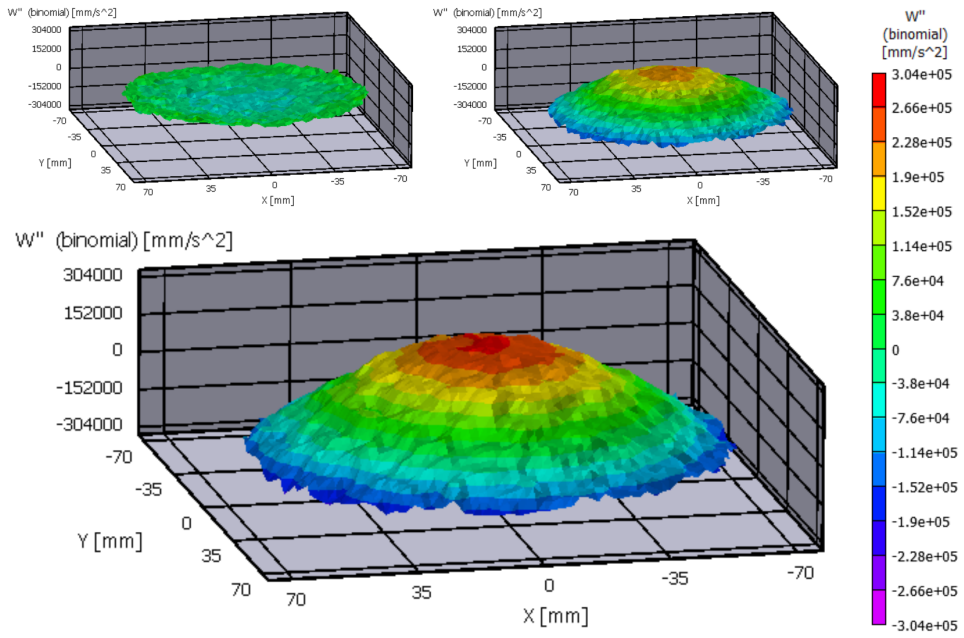

Figure 3.12: 3D rendering of plate deformation at 2440 Hz taken from FFT analysis of DIC data set

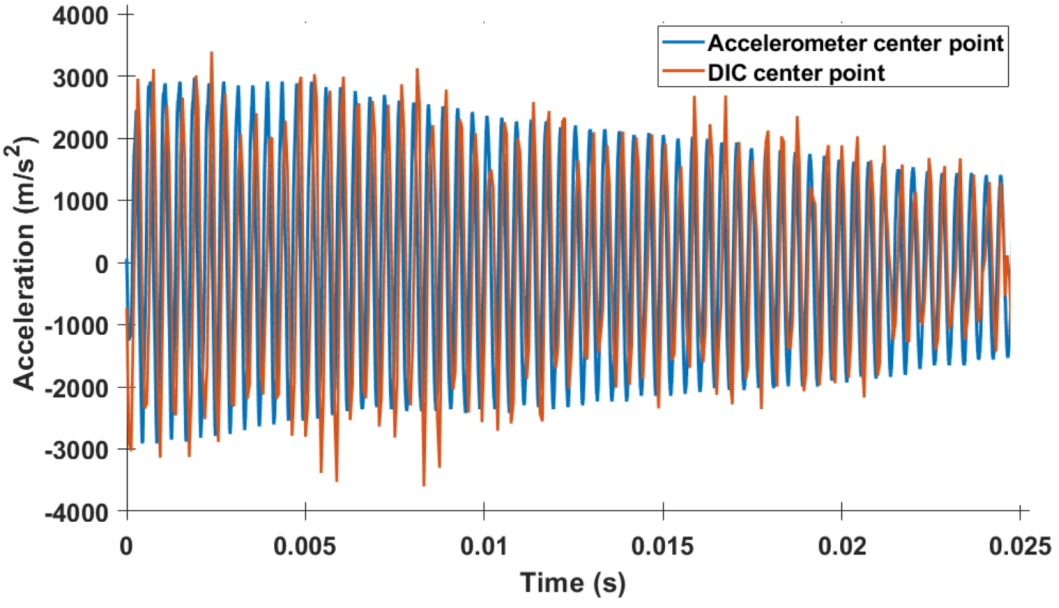

Figure 3.13: Acceleration history collected by DIC tracking of center point overlayed with acceleration history collected by accelerometer

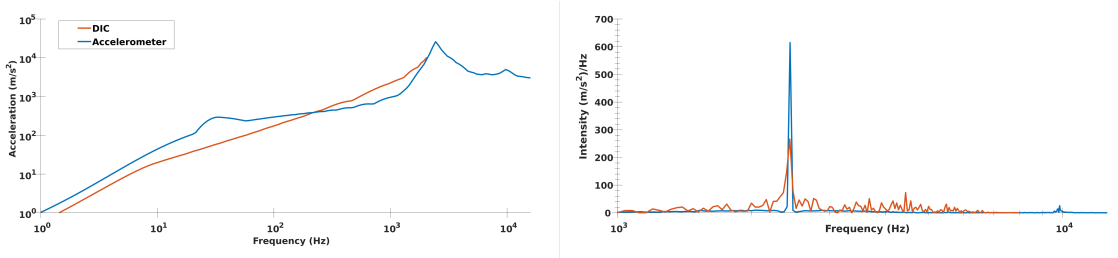

Figure 3.14: SRS profiles of accelerometer data and acceleration determined from position tracking in DIC data on the left. Overlayed FFT of acceleration histories collected from DIC position tracking and accelerometer on the right.

The acceleration histories in Figure 3.13 shows the DIC measurement of the plate center acceleration history in red and the accelerometer data in blue. The tracked acceleration history was processed using SRS and FFT same as the accelerometer data in Figure 3.14. The FFT of the center point on the plate indicated a primary frequency peak at 2440 Hz, coinciding with the FFT of the acceleration history collected by the accelerometer. Comparing the extracted acceleration history from DIC to the acceleration measured directly, both accelerations are in agreement. Accelerometer SRS produces a peak at 2435 Hz agreeing with the peak observed in the FFT of both histories at 2442 Hz seen in Figure 3.13. The SRS of the extracted acceleration history does not indicate any peaks, nor does it display responses above 2000 Hz. The reasoning is likely due to the required sample rates for using the SRS method in this work requiring sampling 10 times faster than the highest frequency of interest in the SRS. The frame rates of the cameras used for DIC were at 16000 fps in order to maintain a high-resolution image for analysis with VIC-3D.

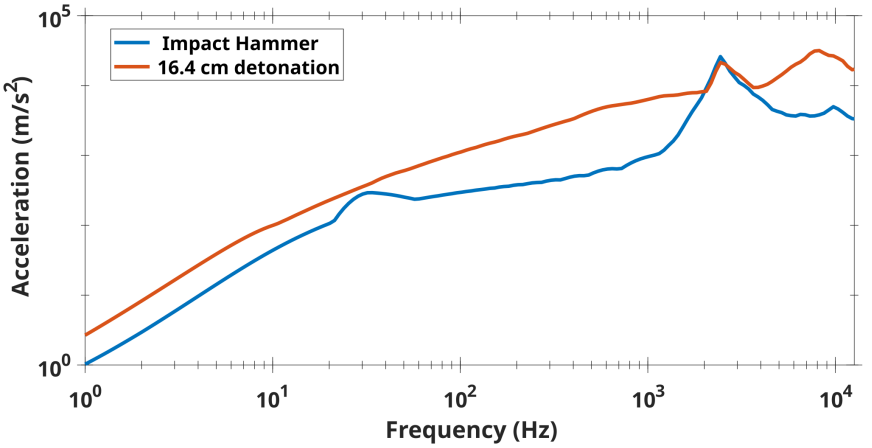

Figure 3.15: SRS profiles of circular plate generated from impact hammer and shock wave from PETN at 16.4 cm standoff. Two primary peaks are present in both methods, with a common peak at 2435 Hz.

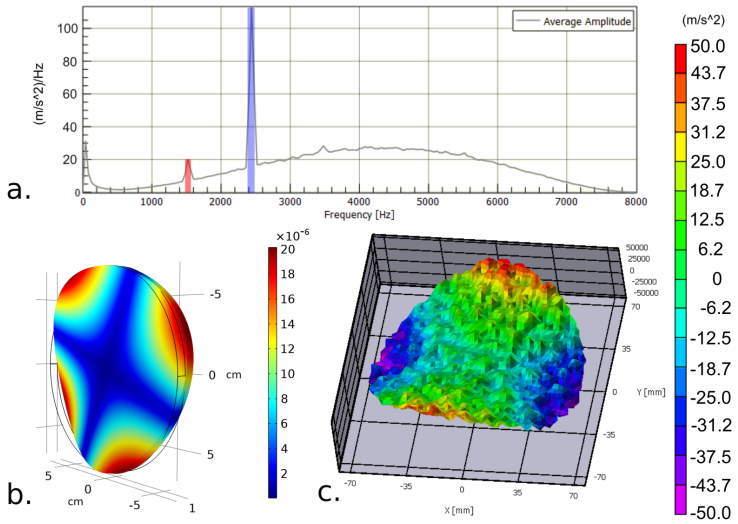

Figure 3.16: (a) Shows the FFT of plate surface from DIC with a 1521 Hz peak indicated by red and a 2440 Hz peak in blue. (b) Is the mode shape at 1647 Hz determined by FEA. (c) Is the surface acceleration of the plate of 1521 Hz peak using VIC-3D.

Examination of the average FFT taken from DIC data of the complete plate shows a secondary peak at 1521 Hz. This weak secondary peak deforms the plate in such a way shown in Figure 3.16c, that any acceleration measured directly by the accelerometer would be minimal and should be considered noise. The accelerometer FFT does display a slightly raised point at 1531 Hz, but an amplitude less than 2% of the 2440 Hz peak.

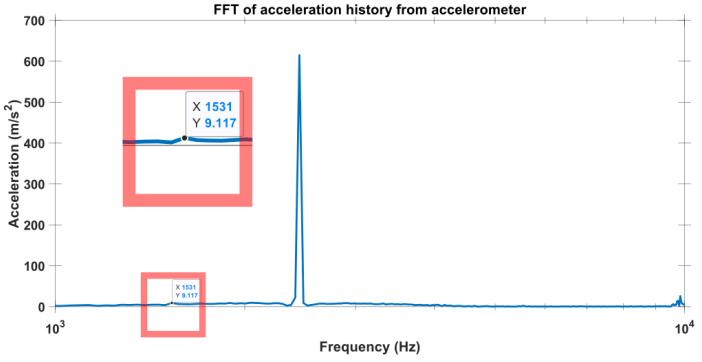

Figure 3.17: Accelerometer data FFT with zoom-in of 1531 Hz outlined in red

The comparison of SRS profiles from impact hammer and shock wave tests is shown in Figure 3.15. The two loading methods display a peak at 2435 Hz and secondary peaks at 8192 Hz and 9742 Hz for the shock wave and impact hammer sources respectively. The amplitude of the peak at 2435 Hz for the impact

hammer is 22% greater than that of the shock wave SRS. The secondary peak amplitude of the shock wave test is greater than the impact hammer peak by a factor of 5. The variation between these loading conditions is in the amplitude at higher frequencies. With the shock wave providing higher accelerations at higher frequencies and impact hammer being better suited for more focused frequencies.

3.4 Uncertainty Propagation

The majority of uncertainty in these tests originates from voltage variance introduced by instrumentation. The manufacturer has reported temperature dependence of the 7270 families of accelerometers has a rate of $-\%0.12/C^o$ from the specified reference temperature of 24 C^o. Included with the temperature dependency, is the voltage deviation unique to each accelerometer provided in the NIST calibration sheet from Endevco and these values can be found in Table 3.5. Applying these uncertainties to the voltages is done before data was processed using the filter described in Equation 2.2.

Table 3.5: Accelerometer models used and variance

Model Number	7270A-2K	7270AM7-6K	7270A-60K
Uncertainty %	1.9	1.9	1.7

CHAPTER 4

CONCLUSION

4.1 Summary and Conclusion

Response spectra from the plate and assembled hemisphere consistently shared multiple frequency peaks between stand off distances for PETN detonation tests. These peak frequencies appear to be dependent on test article geometries as both plate and hemisphere were manufactured from 1018 mild steel and underwent similar loading conditions. The use of FEA to determine modal responses with deformation of the test article confirmed the presence of mode shapes with frequencies near those obtained from SRS calculations of PETN tests. A table of corresponding frequencies for plate and assembled hemisphere geometries in the PETN detonation tests and FEA can be found in Table 4.3.

Table 4.1: Response accelerations in m/s^2 from SRS profiles of the assembled hemisphere shock wave loading tests at varying standoff distances and frequencies of interest.

Standoff	Frequency (Hz)				
(cm)	1218	2734	3251	5468	9741
10.5	2299	4815	5162	24358	43464
15.5	1000	912	577	673	5803
16.4	963	7949	8352	6910	39028
16.7	3482	3312	4807	7226	33665
30.0	5198	3149	2892	3081	16574

Standoff (cm)	Frequencies (Hz) 2435	9742
	Acceleration (m/s)	
14.7	9495	30308
15.0	2987	4167
16.4	21377	26594
16.6	15097	13127
20.0	1850	1670

Table 4.2: Summary of response accelerations from SRS profiles of circular plate shock wave loading tests at varying standoff distances and frequencies of interest.

A summary of the SRS frequency peaks, response accelerations and at which standoff distance is shown in Table 4.1 for the assembled hemisphere and Table 4.2 for the plate test article. It is expected the resulting accelerations would decrease with standoff distance as the nearer standoffs impart a greater impulse on the test article. Both test articles display this trend of decreasing acceleration as standoff increases at the higher frequency 9741 Hz. The outliers being the acceleration of the 15.5 cm and 15.0 cm standoffs for the hemisphere and plate respectively. For the hemisphere this trend is also present at 5468 Hz with the 15.5 cm outlier still present.

The observed modal responses for the assembled hemisphere shared multiple frequencies with the plate and isolated hemisphere. The mode shapes of the isolated hemisphere displaying deformation affecting the inserted plate motion were of interest and presented in the results section for FEA in Figure 3.9 and Table 4.3. The SRS peaks seen in the assembled hemisphere but not in the plate test article are inferred to be influenced by the modal response of the isolated hemisphere from the plate geometry.

Successful extraction of an acceleration history through imaging methods such as DIC greatly benefits the analysis of acceleration. Obtaining measurements by these means removes the influence of instrumentation directly mounted to the test articles and allows for a full field acceleration mapping of the surface. Comparison of the acceleration history from DIC data and accelerometer data were in good agreement. The resulting FFT from each method also showed promise. The caveat is the balance between high-resolution DIC at a lower sample rate or a higher sample rate at a lower resolution. The use of DIC for the measurement of acceleration histories seems promising and will require future research to validate.

Further validation of mode shapes for individual components was performed using DIC on the plate geometry during impact hammer tests. The DIC analysis resulted in the presence of a response at 2440 Hz shown in Figure 2.15 with deformation similar to the mode shape at 2411 Hz using FEA from Figure 3.8. The close proximity of the frequencies observed in SRS, FFT, FEA, and DIC supports the hypothesis that the SRS of complex geometry can be broken down into the SRS of its constituent parts. The SRS profiles of the assembled hemisphere

during shock wave tests share peaks at frequencies near modal frequencies with deformations at locations measured by accelerometers. The investigation of the presence of these peak frequencies near modal frequencies should be further investigated.

Table 4.3: Frequencies peaks obtained from SRS, FEA, and FFT analyses of plate and assembled hemisphere test geometries.

Geometry	Frequency from test scenario FFT (Hz)	PETN SRS (Hz)	FEA (Hz)
Plate	2400	2435	2411
Plate	9700	9742	9950
Assembled Hemisphere	1200	1218	1145
Assembled Hemisphere	-	5468	5430
Assembled Hemisphere	9800	9742	9691
Isolated Hemisphere	-	-	1328
Isolated Hemisphere	-	-	2749
Isolated Hemisphere	-	-	3133
Isolated Hemisphere	-	-	5556

The inclusion of FFT as a method of data analysis was for determining frequency peaks with no emphasis on the amplitudes of each frequency. These frequencies of interest from FFT were then compared to SRS frequency peaks as a second method for determining frequencies of interest.

4.2 Future Work

Further validation of modal responses for differing geometries would benefit from the continued use of DIC and FEA methods. For DIC measurements, focusing on specific regions at a lower resolution and higher frame rates will increase the upper bound frequency of DIC analyses [3]. Analysis of these regions of interest can be analyzed for modal responses with rotational deformation as shown in Figure 4.1. Acceleration collection on regions of rotational deformation

may be challenging. Strain gauges may be better suited for directly measuring rotational deformations.

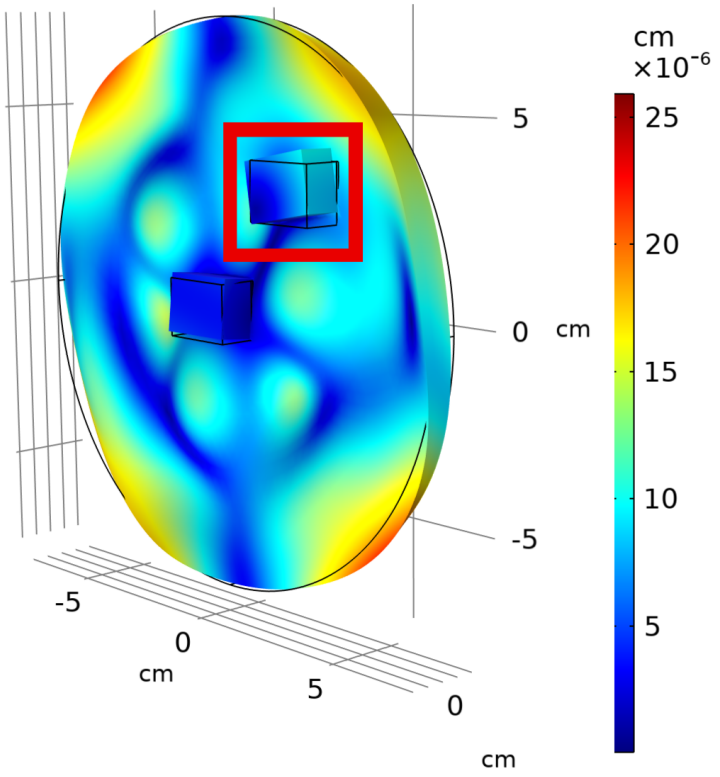

Figure 4.1: Modal response of plate at 912 Hz displaying rotational deformation at accelerometer mount location outlined in red

Continued work with larger test articles would provide optimal spacing for a grid array of accelerometer locations. Integration of accelerations of the array provides an estimate of the full surface displacement. The estimated surface displacement can be compared to displacements of modal responses from FEA and DIC.

The method of calculating modes displayed in this work was performed using COMSOL Arnoldi package (ARPACK) method [19]. Modal frequencies determined by FEA can be confirmed using a second eigenvalue calculation method or FEA package. A secondary method of modal frequency calculation in COMSOL uses FEAST [18]. Initial comparison of these two methods for frequencies between 1 Hz - 1 kHz indicated no variation in frequencies calculated and deformations of the plate geometry. Performing these modal analyses using ANSYS or Simscale would further validate the reported modal frequencies in this work.

Modal frequencies of a structure are expected to influence a structure's response to loading conditions as discussed in [32]. As for the influence of modal responses of individual components this has been investigated by Moldenhauer

[22]. Moldenhauer researched modal coupling using Hilbert spectral analysis to better understand the influence of component responses in non-linear systems. The limited literature found on the application of SRS on sub structure responses reinforces the necessity of validating the presence of component modal responses in SRS profiles of assembled systems.

BIBLIOGRAPHY

[1] J. Edward Alexander. "Alexander - Shock Response Spectrum – A Primer". In: *Sound and Vibration* (2009), pp. 6–14.

[2] Vesta I Bateman, Harry Himelblau, Ronald Merritt, and Jacobs Engineering. "Validation of Pyroshock Data". In: *Journal of the IEST* 55.1 (2012).

[3] Rory Bigger, Benoît Blaysat, Christofer Boo, Manuel Grewer, Jun Hu, Amanda Jones, Markus Klein, Pascal Lava, Mark Pankow, Kavesary Raghavan, Phillip Reu, Timothy Schmidt, Thorsten Siebert, Micah Simonsen, Andrew Trim, Daniel Turner, Alessandro Vieira, and Thorsten Weikert. *A Good Practices Guide for Digital Image Correlation*. Ed. by Elizabeth Jones and Mark Iadicola. 2018. DOI: 10.32720/idics/gpg.ed1/print.format. URL: http://idics.org/guide/.

[4] Maurice Biot. "Transient oscillations in elastic systems". PhD thesis. Pasadena: California Institute of Technology, 1932. DOI: 10.7907/ZHSH-T443.

[5] Anders Brandt. *Noise and Vibration Analysis : Signal Analysis and Experimental Procedures*. Hoboken, UNITED KINGDOM: John Wiley & Sons, Incorporated, 2011. ISBN: 9780470978177. URL: http://ebookcentral.proquest.com/lib/nmt-ebooks/detail.action?docID=792461.

[6] COMSOL. *COMSOL Eigenfrequency study*. 2023. URL: https://doc.comsol.com/5.6/doc/com.comsol.help.comsol/comsol_ref_solver.32.023.html.

[7] Paul W. Cooper. *Explosives Engineering*. Wiley, 2018. ISBN: 9781119537137.

[8] Correlated Solutions. *Vic-3d Software Manual*. Columbia, 2022.

[9] Correlated Solutions. *VIC-3D Testing Guide*. Columbia, 2022.

[10] Guosong Feng, Guang Yang, Jiang Yang, Gongbo Ma, Rui Wang, and Chuang Liu. "Acquisition and Analysis Technology of Pyroshock Response on Spacecraft". In: *Journal of Physics: Conference Series* 1877.1 (2021), p. 012023. ISSN: 1742-6588. DOI: 10.1088/1742-6596/1877/1/012023. URL: https://iopscience.iop.org/article/10.1088/1742-6596/1877/1/012023.

[11] M.J. Hargather and G.S. Settles. "Laboratory-scale techniques for the measurement of a material response to an explosive blast". In: *International Journal of Impact Engineering* 36.7 (2009), pp. 940–947. ISSN: 0734743X. DOI: 10.1016/j.ijimpeng.2008.12.008. URL: https://linkinghub.elsevier.com/retrieve/pii/S0734743X08003266.

[12] Michael J. Hargather and Gary S. Settles. "A comparison of three quantitative schlieren techniques". In: *Optics and Lasers in Engineering* 50.1 (2012), pp. 8–17. ISSN: 01438166. DOI: 10.1016/j.optlaseng.2011.05.012. URL: https://linkinghub.elsevier.com/retrieve/pii/S014381661100159X.

[13] Cyril M. Harris and Allan G. Piersol. *Harris' shock and vibration handbook*. McGraw-Hill, 2002. ISBN: 0071370811.

[14] François M Hemez and Scott W Doebling. "From shock response spectrum to temporal moments and vice-versa". In: *21st International Modal Analysis Conference, Kissimmee, FL*. 2003.

[15] Tom Irvine. *A mean filter method for removing saturation from pyrotechnic shock pulses*. Albuquerque, 2008.

[16] Tom Irvine. *An introduction to the shock response spectrum Revision S*. Albuquerque, 2012.

[17] ISO Central Secretary. *Mechanical vibration and shock — Signal processing — Part 4: Shock-response spectrum analysis*. en. Tech. rep. ISO 18431-4:2007. Geneva, CH: International Organization for Standardization, 2007.

[18] James Kestyn, Eric Polizzi, and Ping Tak Peter Tang. "FEAST Eigensolver for non-Hermitian Problems". In: (2015). URL: http://arxiv.org/abs/1506.04463.

[19] Richard B Lehoucq, Danny C Sorensen, and Chao Yang. *ARPACK users' guide - solution of large-scale eigenvalue problems with implicitly restarted Arnoldi methods*. Software, environments, tools. SIAM, 1998, pp. 1–142. ISBN: 978-0-89871-407-4.

[20] Yongtao Lyu. *Finite Element Method*. Springer Nature, 2022. ISBN: 978-981-19-3362-2. DOI: 10.1007/978-981-19-3363-9. URL: https://link.springer.com/10.1007/978-981-19-3363-9.

[21] Justin N. Martin, Andrew J. Sinclair, and Winfred A. Foster. "On the shock-response-spectrum recursive algorithm of Kelly and Richman". In: *Shock and Vibration* 19.1 (2012), pp. 19–24. ISSN: 10709622. DOI: 10.3233/SAV-2012-0613.

[22] Ben Moldenhauer, Aabhas Singh, Phil Thoenen, Daniel Robert Roettgen, Benjamin Robert Pacini, Robert J. Kuether, and Matt Allen. "Influences of modal coupling on experimentally extracted nonlinear modal models." In: (2018). ISSN: 2191–5644. DOI: 10.1007/978-3-030-12391-8_25. URL: https://www.osti.gov/biblio/1593037.

[23] Bing Pan. "Digital image correlation for surface deformation measurement: historical developments, recent advances and future goals". In: *Measurement Science and Technology* 29.8 (2018), p. 082001. ISSN: 0957-0233. DOI: 10.1088/1361-6501/aac55b. URL: https://iopscience.iop.org/article/10.1088/1361-6501/aac55b.

[24] Bing Pan. "Recent progress in digital image correlation". In: *Experimental mechanics* 51 (2011), pp. 1223–1235.

[25] Eric Polizzi. *FEAST Eigenvalue Solver v4.0 User Guide*. 2020.

[26] P L Reu and T J Miller. "The application of high-speed digital image correlation". In: *The Journal of Strain Analysis for Engineering Design* 43.8 (2008), pp. 673–688. ISSN: 0309-3247. DOI: 10.1243/03093247JSA414. URL: http://journals.sagepub.com/doi/10.1243/03093247JSA414.

[27] Gary S Settles. *Schlieren and shadowgraph techniques: visualizing phenomena in transparent media*. Springer Science & Business Media, 2001. ISBN: 9783540661559.

[28] David Ora Smallwood. *Improved recursive formula for calculating shock response spectra*. Tech. rep. SAND-80-1315C. Albuquerque: Sandia National Laboratories, 1980.

[29] M D Trifunac. "70-TH Anniversary of Biot spectrum". In: *ISET Journal of Earthquake Technology, Paper No* 431.1 (2003), pp. 19–50.

[30] D Z Turner. *An overview of the stereo correlation and triangulation formulations used in DICE*. Tech. rep. SAND2017-1875R. Albuquerque: Sandia National Laboratories, 2017.

[31] Patrick Walter. "Accelerometer limitations for pyroshock measurements". In: *Sound and Vibration* 43.6 (2009), pp. 17–19.

[32] Jaap J. 1944- Wijker. *Mechanical vibrations in spacecraft design*. English. Berlin ; Springer, 2004. URL: http://catdir.loc.gov/catdir/enhancements/fy0817/2003060644-d.html.

[33] Kyle Oakley Winter. "Irregular reflections of unsteady shock waves". PhD thesis. Socorro: New Mexico Tech., 2021.

APPENDIX A

PETN PRESSING TEST PLAN

NEW MEXICO TECH
ENERGETIC MATERIALS RESEARCH AND TESTING CENTER
1001 South Road • Socorro • NM • 87801 • telephone: 575.835.5312 • facsimile: 575.835.5630 • www.emrtc.nmt.edu
EMRTC - Committed to Excellence in the Fields of Energetic Materials Research, Testing and Training since 1947.

TEST PLAN

TP-20-33

Shock Response Study
Revision

New Mexico Tech Mech. Eng.
Dr. Michael Hargather
Michael.Hargather@nmt.edu

Author: James Reeves
(505) 307-3115
James.Reeves@student.nmt.edu

Fund: MBSS20

Date: 04/15/2021
Revision 1: 06/17/2021
Revision 2: 08/17/2022
Revision 3: 12/06/2022

1. **Purpose:**
   Explosive tests will study the shock propagation around steel plates of varied shapes. Gram scale spheres of pentaerythritol tetranitrate (PETN) will be detonated to generate a shock wave which will impinge on or pass over the test plate. The shock wave will be visualized by refractive imaging and the acceleration from the shock wave will be measured by accelerometers on the test plate.

2. **Test Overview/Summary:**

   2.1. The gram scale PETN pellets will be remotely pressed from loose powder in the West laboratories. A measured amount of loose commercially manufactured PETN powder will be inserted into the bottom half of the pellet die. The top half of the die will be inserted, and the die compressed remotely using a 20-ton hydraulic press until the mechanical stop is reached. The pressure will then be removed, and the die reconfigured for extraction. Extraction will either occur under the weight of the die or remotely using the hydraulic press.

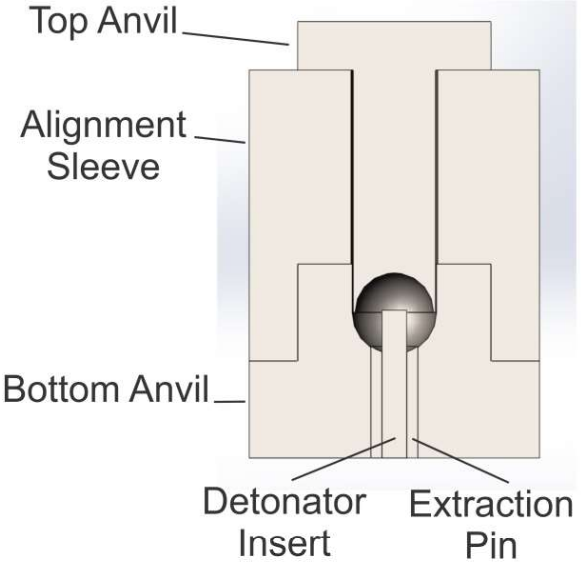

Figure 1: Cutaway diagram of pellet pressing die.

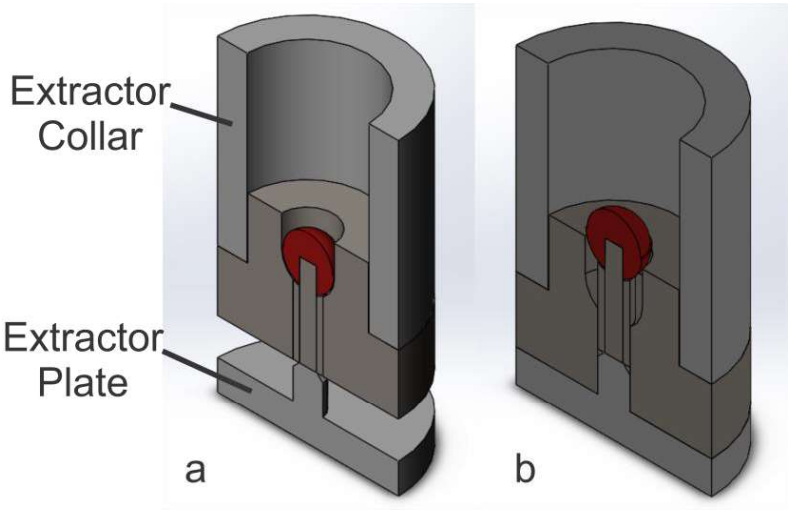

Figure 2: Cutaway diagram of explosive pellet being extracted from die.

2.2. The pressed PETN pellets will be primed by the addition of a RP-3 detonator inserted into charge cavity. One drop of cyanoacrylic glue (super glue) will be used to secure the detonator to the pellet.

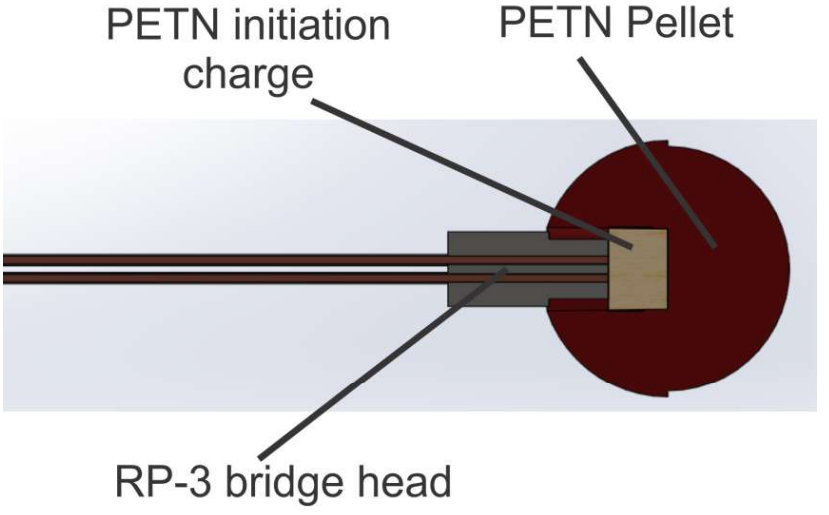

Figure 3: Cutaway diagram of explosive pellet being extracted from die.

2.3. In the experimental setup, the PETN charge will be detonated at various distances from the target plate within the Ballistics Sciences Laboratory (BSL). The charge will be suspended by the lead wires of the EBW and secured to the explosive gantry. The

distance of the charge from the target plate will be measured before each test. The target plate will be suspended from the three eyehooks attached radially outward every 120˚.

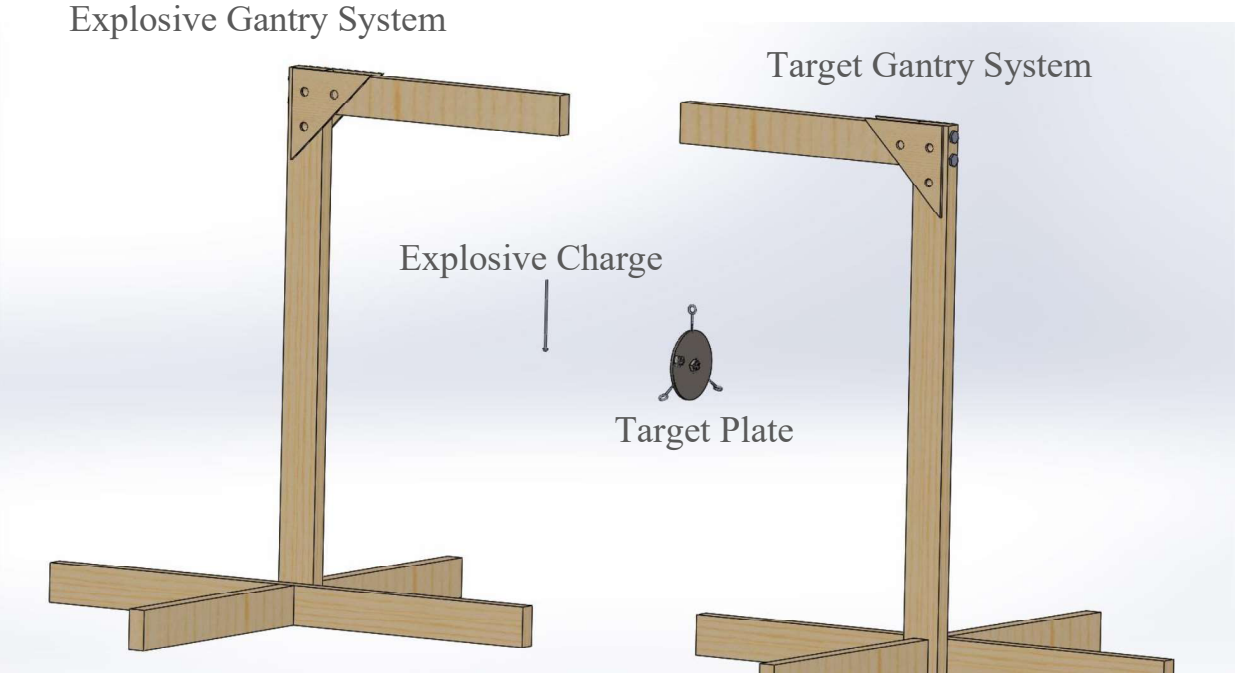

Figure 3: Labeled diagram of hanging target and charge

2.4. The shock wave generated by detonating the PETN pellets will be visualized with at least one refractive imaging system assembled and operated by the Shock and Gas Dynamics Lab (SGDL), Dr. Hargather's laboratory group. The system will consist of two 1-foot mirrors, a high-speed camera and a light source. During setup, a LED light system will be used for system alignment. During system checks and testing the light source will be the SI-LUX 640 laser system which is a Class 3b laser.

2.5. Testing will take place near the NW bay door, approximately 50 feet from fire set .

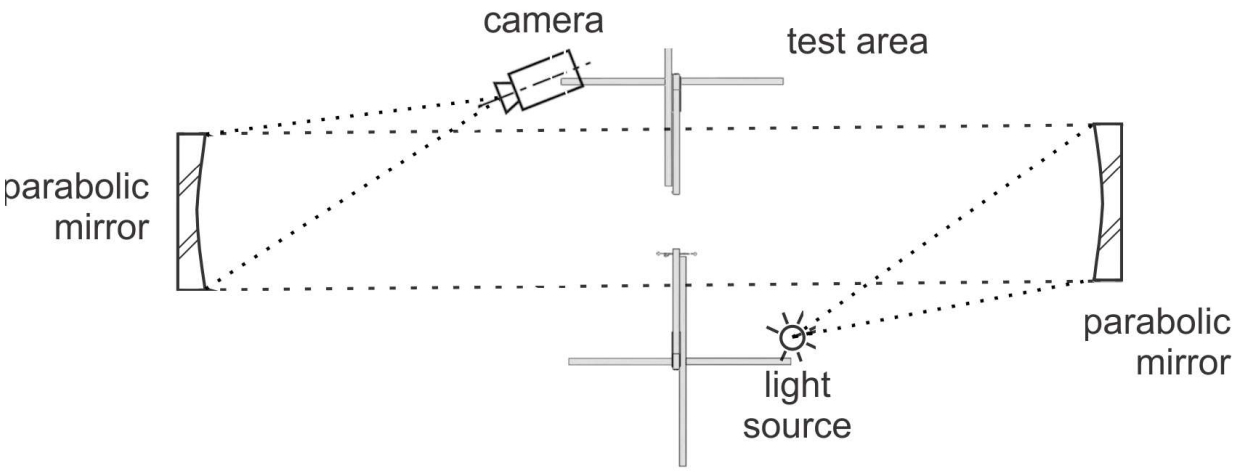

Figure 4: Top-down view of setup with light ray diagram shown.

2.6. Additional high-speed cameras may be used to record the test event. These cameras will be provided and operated by SGDL.

2.7. Accelerometers will be mounted on the target plate to record the acceleration experienced by the target plate. The accelerometers will record the shock response will be provided by SGDL.

2.8. Photon Doppler Velocimetry (PDV) will be applied to measure the particle velocity of the sample as the shock wave propagates through it. The PDV system will be provided and operated by SGDL.

3. Location of Test:

3.1. PETN pressing and priming by the addition of an RP-3 will be conducted at the West laboratories sample preparation room.

3.2. The pellet will be detonated in the BSL near the NW bay door

4. Sequence of Steps: (See Attachment 4 for checklist)

5. Test Matrix:

5.1. Table 1 outlines initial test series. Future tests will vary in charge distance, geometry of target plate and explosive load will remain the same. Future tests matrices will be updated prior to tests.

Test #	Type of Test	Data Requirements	Energetics
1			1 gram PETN pellet RP-3 EBW
2			1 gram PETN pellet RP-3 EBW
3			1 gram PETN pellet RP-3 EBW
4-7			1 gram PETN pellet RP-3 EBW

Table 1 – Test Matrix

6. Construction: (non-standard items only)

6.1. Pressing die and optical systems will be provided by SGDL

6.2. Provided by SGDL

6.2.1. Pressing die

6.2.2. Optical systems

6.2.3. Accelerometers

6.2.4. PDV System

7. Firing Detail Schematic:

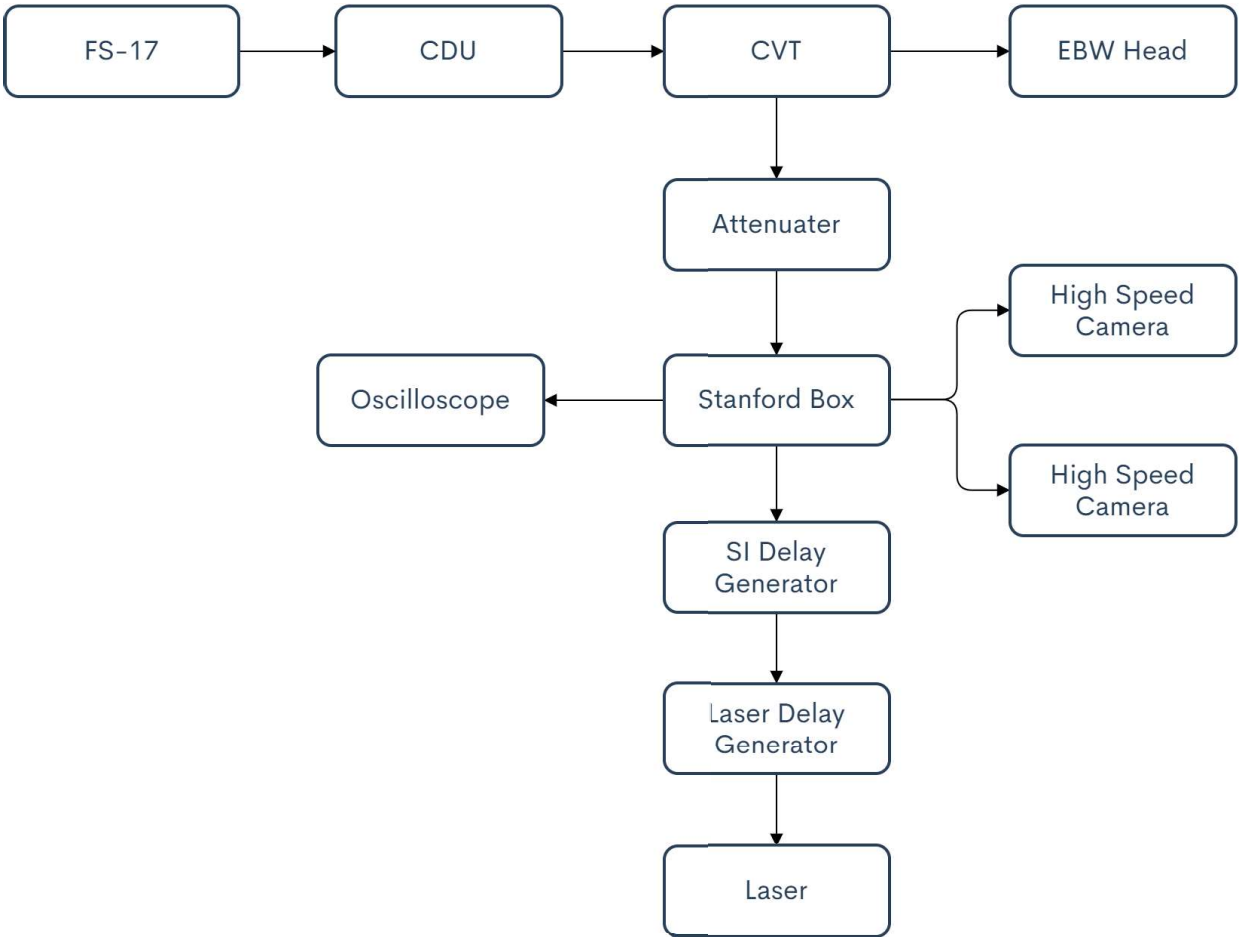

Figure 5: Firing Schematic.

8. Energetic Materials:

8.1. PETN powder: Each pellet will be pressed from 1 gram of PETN

8.1.1. In addition, each pellet will be primed a RP-3 bridge head

8.1.2. Total of 7 pellets will be pressed

8.2. RP-81 detonators

8.2.1. RP-81 will only be used in event of misfire

9. Instrumentation:

9.1. Oscilloscope, accelerometers and PDV system

9.2. The accelerometers and signal conditioners provided by SGDL

9.2.1. 2 accelerometers rated up to 60 000 g

9.2.2. 1 accelerometer rated up to 6 000 g

9.2.3. 4 handheld amplifier and signal conditioners

9.3. High Speed cameras, provided by SGDL

10. Specific Tools and Equipment: (Includes specialty tools, heavy equipment, Fire Sets, etc.)

10.1. FS-17 fire set

10.2. 20 Ton Press

10.3. SI-LUX 640 Laser

10.4. PDV Laser

10.5. Shimadzu and Photron cameras

11. Documentation: (Includes videos, reports, etc.)

11.1. High speed video

11.2. Shock response data

11.3. Still images

11.4. Written notes

11.5. Safety cameras

12. Instructions for Spill Cleanup and Disposal of any Scrap and Waste A&E: (if different than those listed in Attachment 2)

13. Specific Hazards: (Include hazards in Safety Data Sheets (SDS))

13.1. Fire

13.2. Explosion

13.3. High voltage

13.4. Laser illumination

13.5. Static EMR

14. PPE Required: (As determined by JHA; include setup, test and post-test operations)

14.1. Laser safety glasses rated at OD5 or greater for 640 nm. Required within the building whenever laser key is inserted.

14.2. Laser safety glasses rated at OD2 or higher for 1550 nm. Required within a 10-foot radius of active PDV probes. OD2 glasses not required when outside of 10-foot radius

14.3. Hearing protection

14.4. (Pressing) Cotton clothing

14.5. (Pressing) ESD wrist straps

15. Emergency Procedures: (if different than those listed in Attachment 2)

16. Proposed Test Schedule:

TRR –

Test Preparation – Prior to

Test walkthrough – Prior to test date

Pressing PETN pellets –

Testing with shown configuration –

Post Test Operations – After

17. References: (Include all references pertinent to the project/test)

- DoD 4145.26-M, DoD Contractors Safety Manual for AA&E
- SOP 101, Health and Safety
- SOP 102, Field Laboratory Safety
- SOP 103, Industrial Safety
- SOP 108, HAZCOM Program
- SOP 201, Grounding Procedures
- SOP 202, Initiation of Energetic Materials
- SOP 203, Arms, Ammunition and Explosives Procedures
- SOP 402, Emergency Action Plan
- SOP 403, Risk Management
- SOP 500, COVID-19 Procedures
- LLNL-TR-520411, PETN Sample Preparation Safety Limits
- SI-LUX 640 User Guide
- SI-LUX 640 Data Sheet

18. Attachments:

1. Job Hazard Analysis
2. Safety and General Requirements
3. Site Closure Map
4. Test Checklist
5. Tailgate Briefing Form
6. Safety Data Sheets
7. PETN Sample Preparation Safety Limits, LLNL-TR-520411
8. SI-LUX 640 User Guide

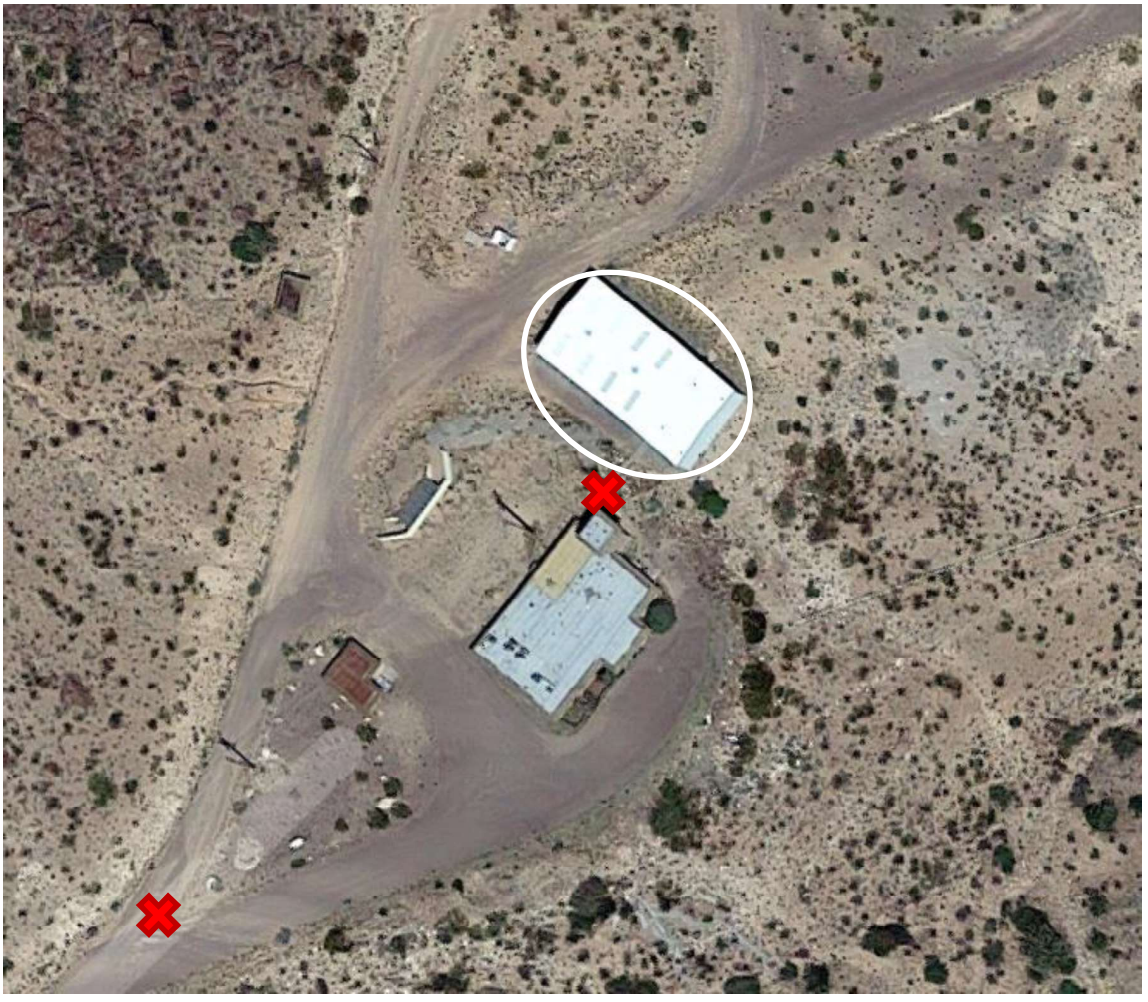

- Testing will take place inside of BSL, indicated by the white outline
- Z signs will be located at the stairs between BSL and Torres and entrance to Torres and BSL. Indicated by the Xs on the map.

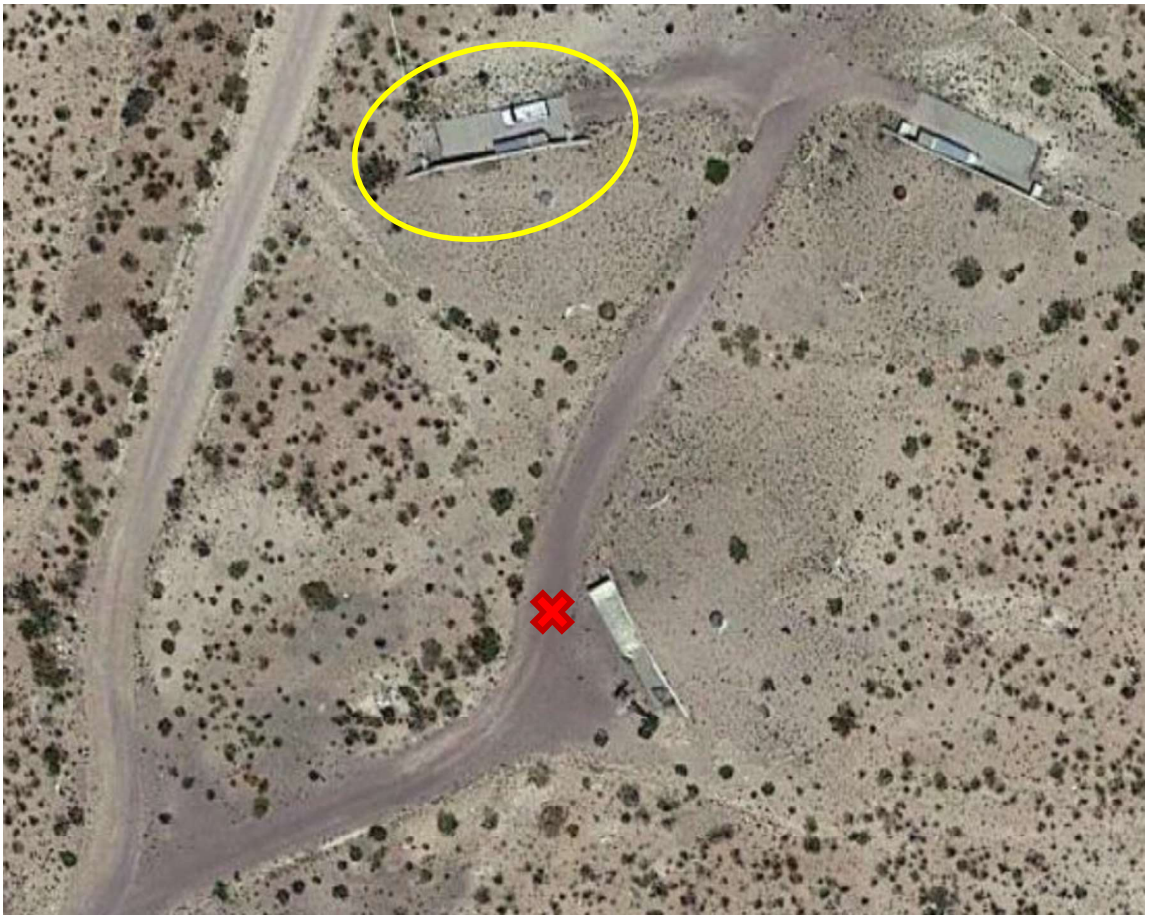

- Pressing of PETN will be located in West Lab indicated by the yellow oval
- Z sign will be located at East and West Lab entrance, indicated by red X

Attachment 4

Test Checklist

START OF DAY PRETEST SHEET FOR Shock Response Study

1.1. Testing Conditions and Safety:

1.1.1. Test Engineer: _____

1.1.2. Ordnance: _____

1.1.3. Operator Safety: _____

1.1.4. Personnel present: _____
_____

Total persons present: _____

1.1.5. Note date/time: _____

1.1.6. Check that a Z-sign is on entry road to BSL facility, a Z-sign is in place at the start of the stairs to the Ballistics Science Building (BSL) and at the parking area on the south of BSL

1.1.7. Barometric pressure (inHg):_____

1.1.8. BSL inside temperature:_____

1.1.9. Number of planned tests:_____

1.2. Safety Briefing:

1.2.1. Review hazards present on site during testing and required personnel protective equipment (PPE) as specified by the PPE survey and JHA

1.2.2. Distribute PPE (at a minimum hearing protection and safety glasses) to all personnel to be present during testing

1.3. Signatures of Responsible Parties:

1.3.1. Test Engineer: _____

1.3.2. Ordnance: _____

1.3.3. Operator Safety: _____

2. PELLET PRESSING PROCEDURES

All procedures will have a walkthrough with Dr. Hargather or his designated representative prior to pressing operations and testing.

In the event of anything unusable or unexpected during the pressing of explosives the engineer/test manager and the ordnance technician will contact the Ordnance Supervisor

and Safety Officer, or their designated representatives, to inform them of the event and to discuss troubleshooting options.

2.1. Setup

Designate safe area from where the press can be remotely operated. Inside bunker adjacent to West lab.

2.1.1. A designated safety observer will be briefed, name recorded and provide a signature.

2.1.2. Ensure hydraulic press is grounded and all personnel handling explosives are following appropriate static safety procedures (SOP 201)

2.1.3. Position the bottom bed of the hydraulic press at the second position from the top.

2.1.4. Secure pressing surface to bottom bed by using guide rods.

2.1.5. Ensure guide rods are tightened and scale bed is able to freely travel in direction of press. (Refer to figures 1 and 2 for steps 2.1.5 and 2.1.6)

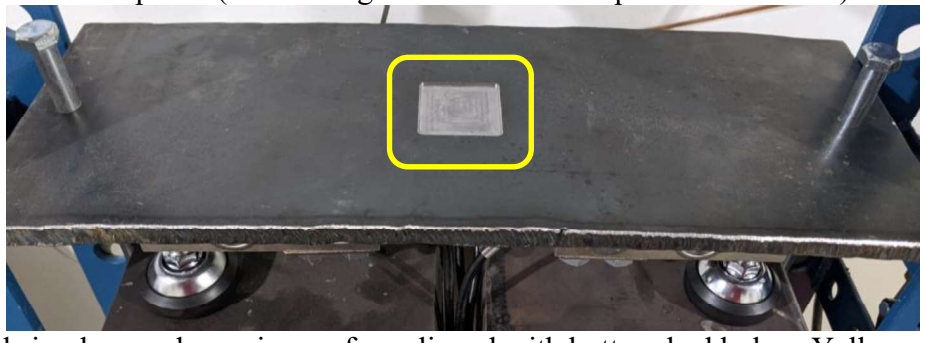

Figure 1: Guide rods in place and pressing surface aligned with bottom bed holes. Yellow outline indicates alignment groove location.

Figure 2: Side view of guide rod once secured to bottom bed and rod fed through holes in scale bed.

2.1.6. Check that the pressure release value for the hydraulic press is in the closed position (ready for pressing)

2.1.7. Place an air compressor in the remote operation area.

2.1.8. Attach an air hose to the air inlet for the hydraulic press place the other end in the remote operation area. **Do not attach the second end of the hose to the air compressor.**

2.1.9. Place CCTV cameras around the press so that the pressure gauge and die are clearly visible. Place the CCTV monitor in the remote operations area.

2.1.10. Perform a walk though of all steps with ordnance and all test personnel

2.2. Assembling Explosive Pellet Die (refer to Figure 3 and 4 for naming in following sections)

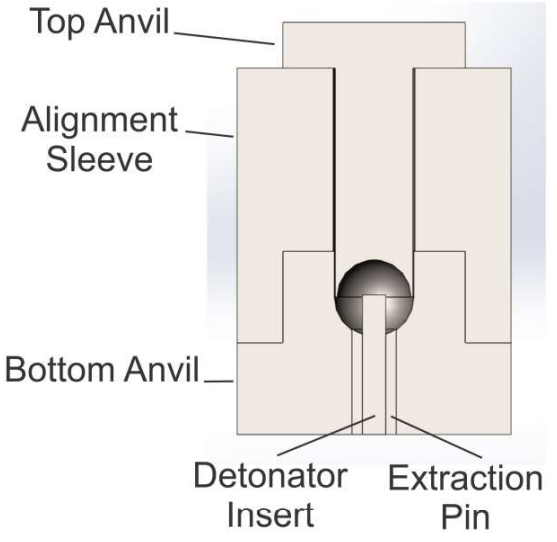

Figure 3: Cutaway diagram of pellet pressing die.

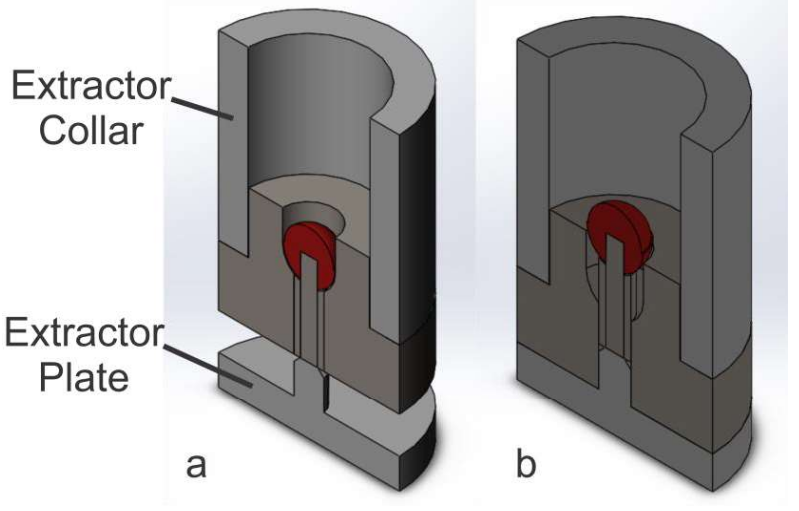

Figure 4: Cutaway diagram of explosive pellet being extracted from die.

2.2.1. Check that CCTV is functioning with video recording of pressing and air hose is detached from air compressor.

2.2.2. Ensure all pieces of the explosive die are moving freely.

2.2.3. Place the bottom anvil on the steel plate on the bottom bed and insert the extraction pin and detonator insert.

2.2.4. Remove all non-essential personal from the work area.

2.3. Pellet press preparations

Only ordnance will approach the die and carry out Sections 2.3 -2.8

2.3.1. Apply a thin layer of mold release to all pressing surfaces of the die.

2.3.2. Measure out the designated amount of explosive for the pellet and carefully pour it in to the bottom anvil.

2.3.3. Remove any powder that spilled onto the mating surfaces between the bottom anvil and alignment sleeve.

2.3.4. Firmly Place bottom anvil into alignment groove, centered on scale bed. (Refer to figure 1)

2.3.5.

2.3.6. Place the alignment sleeve onto the bottom anvil.

2.3.7. Place the manual stop onto the alignment sleeve.

2.3.8. Place the top anvil into the alignment sleeve.

2.4. Pressing Explosive Pellet

Only ordnance will approach the die and carry out Sections 2.3 -2.8

2.4.1. Ensure test area is clear of non-test personnel.

2.4.2. Manually extend the hydraulic press ram until it is nearly in contact to the top anvil.

2.4.3. Manually move the air inlet valve at the base of the hydraulic press to the fixed open position.

2.4.4. All remaining personnel are to retreat to the designated remote operation area.

2.4.5. Attach air hose to air compressor and apply air until the manual stop is reached or max pressure is reached.

2.4.6. Remove the air hose and allow the press to remain under pressure for the designated dwell time of 15 minutes.

2.4.7. After the dwell time has elapsed remove pressure from the press and allow the ram to retract fully.

2.5. Inspecting Pressed Assembly

Only ordnance will approach the die and carry out Sections 2.4 -2.8

2.5.1. In the event of anything unusable or unexpected during the pressing of explosives the engineer/test manager and the ordnance technician will contact the Ordnance Supervisor and Safety Officer, or their designated representatives, to inform them of the event and to discuss troubleshooting options.

2.5.2. Move the air inlet valve at the base of the hydraulic press to the closed position.

2.5.3. Remove the mechanical stop.

2.5.4. Attempt to lift the top anvil.

2.5.5. If the top anvil moves freely then move to Section 2.5.

2.5.6. If the top anvil appears to be lodged or seized move to Section 2.6.

2.6. Extracting Explosive Pellet (Freely Moving)

Only ordnance will approach the die and carry out Sections 2.4 -2.8

2.6.1. Remove the top anvil.

2.6.2. Remove the alignment sleeve.

2.6.3. Lift the bottom anvil and place the bottom anvil on the extractor plate, as shown in Figure 1.

2.6.4. If the weight of the bottom anvil dislodges the pellet, remove the pellet.

2.6.5. If the pellet remains lodged, place the extractor collar on the bottom anvil, as shown in Figure 1. Move onto 2.7 for seized pellet extraction.

2.7. Extracting Explosive Pellet (Seized)

Only ordnance will approach the die and carry out Sections 2.4 -2.8

2.7.1. Lift the bottom anvil and place the bottom anvil on the extractor plate, as shown in Figure 1.

2.7.2. Place the extractor collar on the alignment sleeve.

2.7.3. Move the hydraulic pressure release value for the hydraulic press to the closed position (ready for pressing).

2.7.4. Manually extend the hydraulic press ram until it is nearly in contact to the extractor collar.

2.7.5. Manually close the air inlet valve at the base of the hydraulic press.

2.7.6. All personnel are to retreat to the designated remote operation area.

2.7.7. Attach air hose to air compressor and apply air until the bottom anvil is in full contact with the extractor plate.

2.7.8. Remove pressure from the press and allow the ram to retract fully.

2.7.9. Approach the die and remove the extractor collar and the alignment sleeve.

2.7.10. Remove the pellet from the bottom anvil.

2.8. Priming Explosive Pellet

Only ordnance will approach the die and carry out Sections 2.3 -2.8

2.8.1. Perform Section 2.8 in West laboratories sample preparation room.

2.8.2. Place the pellet in the conical pellet rest to prevent it from rolling.

2.8.3. Insert the RP-3 into the detonator hole and press it in until it contacts the charge.

2.8.4. Apply 1 drop of ordnance approved super glue to the RP-3 to adhere it to the body of the pellet. Apply ordnance approved super glue accelerant to prevent spread of super glue.

2.8.5. If pressing a new pellet start at 2.1.4

3. PRETEST PROCEDURES

3.1. All procedures will have a walkthrough with Dr. Hargather or his designated representative prior to pressing and testing operations

3.2. Start of Day

3.2.1. Ensure Start of Day Pretest Sheet has been properly filled out.

3.2.2. Ensure all personnel have been properly briefed on testing hazards and have received proper safety briefing and PPE.

3.2.3. Ensure laser hazard signs are posted at BSL entrances

3.2.4. Perform a walk though of all steps with ordnance and all test personnel

3.3. System Hardware Checkouts (Camera, Laser system, Accelerometers and PDV system)

3.3.1. Verify that laser system is setup properly as outlined in 'SI-LUX 640 User Guide.

3.3.2. Ensure the laser key is removed and the system is disarmed in the software.

3.3.3. Set the Stanford Box to 'Single Shot' trigger mode.

3.3.4. All personnel without laser safety glasses must evacuate at this point.

3.3.5. Ensure all remaining personnel have laser safety glasses in place.

3.3.6. Ensure proper signal is coming from the PDV laser. If not, correct as needed

3.3.7. Arm PDV laser.

3.3.8. Arm the high-speed camera.

3.3.9. At the direction of the test engineer, arm the laser in the software and loudly announce that the laser is armed.

3.3.10. Insert the key to the laser safety unit and turn it to the 'ON' position. Loudly announce that the key is in and system is on.

3.3.11. Press the 'EXC' button on the Stanford box to trigger the camera and laser.

3.3.12. Turn the key in the laser safety unit to the 'OFF' position and remove the key. Loudly announce that the key is out.

3.3.13. Disarm PDV laser.

3.3.14. If the laser system did not automatically disarm, disarm the laser in the software and loudly announce that the laser is disarmed.

3.3.15. At this point laser safety glasses may be removed and those without laser safety glasses may return.

3.3.16. Ensure all systems triggered.

3.4. Fire System Checkout (Spark Gap)

3.4.1. Ensure the laser key is removed and the system is disarmed in the software.

3.4.2. Place a spark gap in the field of view of the refractive imaging system and wire the spark gap to the fire system.

3.4.3. Set the Stanford Box to 'External' trigger mode.

3.4.4. All personnel without laser safety glasses must evacuate at this point.

3.4.5. Ensure all remaining personnel have laser safety glasses in place.

3.4.6. Ensure proper signal is coming from PDV laser. If not correct as needed

3.4.7. Arm PDV laser.

3.4.8. Arm the high-speed camera.

3.4.9. At the direction of the test engineer, arm the laser in the software and loudly announce that the laser is armed.

3.4.10. Insert the key to the laser safety unit and turn it to the 'ON' position. Loudly announce that the key is in and system is on.

3.4.11. Ensure all personnel are separated from the spark gap.

3.4.12. The test engineer will then hand control over to ordnance to fire the spark gap.

3.4.13. Ordnance fires spark gap.

3.4.14. Disarm PDV system.

3.4.15. Turn the key in the laser safety unit to the 'OFF' position and remove the key. Loudly announce that the key is out.

3.4.16. If the laser system did not automatically disarm, disarm the laser in the software and loudly announce that the laser is disarmed.

3.4.17. At this point laser safety glasses may be removed and those without laser safety glasses may return.

3.4.18. Verify all systems triggered and the spark can be visualized in high speed images.

4. TEST PROCEDURE

(May only begin if Start of Day Pretest Sheet and all system checkouts have been performed.)

4.1. Target Alignment

4.1.1. Target will be suspended vertically with opposing face of accelerometer facing down.

4.1.2. Orient the target such that the normal of the target surface is orthogonal to the cameras field of view (minimize cross sectional area)

4.1.3. Align PDV laser with the target. Personnel within 10 feet of PDV system must be wearing appropriate safety goggles.

4.1.4. Use the live high-speed camera feed as a confirmation of alignment.

4.2. Arming Cameras and Accelerometer system

4.2.1. Ensure the laser key is removed and the system is disarmed in the software.

4.2.2. Arm the cameras and oscilloscope.

4.3. Arming Laser

4.3.1. All personnel without laser safety glasses must evacuate at this point.

4.3.2. Ensure the Stanford Box is set to ‘External’ trigger mode.

4.3.3. Ensure all remaining personnel have laser safety glasses in place.

4.3.4. Ensure proper signal is coming from PDV laser. If not, correct as needed.

4.3.5. Arm PDV laser.

4.3.6. Arm high-speed cameras.

4.3.7. At the direction of the test engineer, arm the laser in the software and loudly announce that the laser is armed.

4.3.8. Insert the key to the laser safety unit and turn it to the 'ON' position. Loudly announce that the key is in and system is on.

4.3.9. All non-essential personnel must retreat to a safe area behind designated barriers.

4.4. Setting Charge

4.4.1. Ensure the target suspension system is in a stable condition.

4.4.2. Pellet will be supported by detonator line.

4.4.3. Direct the spherical side of the charge towards target center line

4.4.4. Ensure the charge is centered in reference to the target and at the desired distance

4.4.5. Turn on safety siren and signal light located on north side of BSL

Laser safety eye protection and hearing protection is required for all remaining steps for all personnel.

Checklist prior to firing

4.4.6. Stanford Box ready to trigger

4.4.7. Oscilloscope prepared to trigger

4.4.8. Cameras set to trigger

4.4.9. PDV ready to trigger

4.4.10. Target is aligned properly

4.4.11. Laser ready to trigger

4.4.12. Ensure all personnel are behind barriers.

4.4.13. The test engineer will then hand control over to ordnance.

4.4.14. Ordnance will connect the bridge wire to fire set.

4.4.15. Ordnance will fire the system.

4.4.16. PDV laser will be disarmed

4.4.17. Ordnance will clear the range and determine when it is safe for test personnel to exit the barriers

4.4.18. Turn off signal light and siren

4.4.19. Turn the key in the laser safety unit to the ‘OFF’ position and remove the key. Loudly announce that the key is out.

4.4.20. If the laser system did not automatically disarm, disarm the laser in the software and loudly announce that the laser is disarmed.

4.4.21. At this point laser safety glasses may be removed and those without laser safety glasses may return.

4.4.22. Save all data to computers

4.5. For repeat tests, return to step 4.1

SHOCK RESPONSE SPECTRA OF SHOCK LOADED HEMISPHERE AND PLATE GEOMETRIES

by

James M. Reeves

Permission to make digital or hard copies of all or part of this work for personal or classroom use is granted without fee provided that copies are not made or distributed for profit or commercial advantage and that copies bear this notice and the full citation on the last page. To copy otherwise, to republish, to post on servers or to redistribute to lists, requires prior specific permission and may require a fee.